UNIVERSITÀ
DEGLI STUDI
DI PADOVA

Sede Amministrativa: UNIVERSITÀ DEGLI STUDI DI PADOVA

Dipartimento di SCIENZE CARDIOLOGICHE, TORACICHE E VASCOLARI

Corso di Dottorato in Scienze Mediche, Cliniche e Sperimentali
Curriculum Neuroscienze
XXIX Ciclo

Tesi di Dottorato

Postprocessing Neuroimaging methods in MRI and PET/MRI

with applications to Multiple Sclerosis and other Neurological diseases

Tesi redatta con il contributo finanziario di Teva Italia Srl.

Coordinatore: Ch.mo Prof. Gaetano Thiene
Supervisore: Ch.ma Prof.ssa Elena Pegoraro
Co-Supervisore: Ch.mo Prof. Paolo Gallo

Valutatori: Ch.ma Prof.ssa Matilde Inglese
Ch.mo Prof. Wolfgang Erb

Dottorando: Dr. Davide Poggiali
Matricola: 1084981

A.A. 2016/17

Ai miei nonni.
***Vittoria** (1922-2004), che ricordo solo cantare, e una volta, ridere.*
***Mario** (1921-2016), presenza silente, paziente, mite. E ultimamente, incline a commuoversi in modo contagioso.*
***Angela** (1942-2009), passionaria, dissennata, generosa e (le piaccia o meno) testimone di fede.*
***Riccardo** (1933-), militante, riflessivo, comunicativo, ha da poco imparato a usare WhatsApp.*

Ringraziamenti

Desidero ringraziare mia moglie Silvia, per la sua pazienza nei miei confronti; ringrazio anche la mia e la sua famiglia di origine, così diverse in (quasi) tutto, ma rispettose e accoglienti per entrambi.

Ringrazio gli amici, dai mateamici fiorentini a quelli padovani.

Ringrazio inoltre chi mi ha dato fiducia in ambito professionale: il mio Relatore di tesi Triennale a Firenze, prof. Villari, che mi ha insegnato l'importanza di cercare un senso profondo al proprio lavoro e mi ha attaccato la passione per le citazioni letterarie; il mio Relatore di tesi Magistrale a Padova, prof. De Marchi, che mi ha sostenuto in tutto quel che ho fatto dalla tesi in poi e mi ha spinto a continuare gli studi con il dottorato di ricerca; il prof. Cecchin, che mi segue dalla Tesi Magistrale e che ancora non si è stancato del sottoscritto; il prof. Gallo che mi ha seguito e incoraggiato costantemente.

Ringrazio inoltre tutti i Colleghi del Centro di Sclerosi Multipla di Padova, del Dipartimento di Neuroscienze e di Neuroradiologia, tutti gli infermieri e la squadra dei tecnici TSRM, che hanno sopportato la mia pur gentile insistenza e cocciutaggine, e senza i quali queste pagine non esisterebbero. Un sentito ringraziamento a tutte segretarie i cui pazienti consigli sono stati un aiuto indipensabile per districarmi fra le maglie delle pratiche burocratiche.

Non posso inoltre non ringraziare i pazienti le cui immagini hanno transitato davanti al mio schermo. La loro sofferenza, che intuisco da queste immagini è per me fonte di paura, perplessità, ma anche di riflessione profonda e di speranza.

List of most used acronyms

AD Alzheimer's Disease
CNS Central Nervous System
CSF CerebroSpinal Fluid
GM Grey Matter (UK, US: Gray Matter)
MRI Magnetic Resonance Imaging
MS Multiple Sclerosis
PET Proton Emission Tomography
WM White Matter

Synopsis

Many non-invasive imaging instruments have been developed in the last 40 years, allowing to obtain images of the interior human body while the patient is still alive. In the context of Neurology studies, imaging systems as CT, MRI, SPECT or PET allows to obtain biomarkers useful to quantitatively distinguish between healthy and unhealthy subjects, evaluate the staging of a Neurological illness in a patient, evaluate the efficacy of a treatment, explore the causes of the illness.
In this work MRI and PET imaging system are introduced from scratch, going from reconstruction from raw data to state-of-the art post-processing techniques and the computation of more popular biomarkers.
After this introduction, three original works using the recent PET/MRI imaging system are presented, with a particular focus on the methods. These three studies involve patients with Multiple Sclerosis, Alzheimer's Disease and Brain Tumor.

Riassunto

Negli ultimi 40 anni sono stati sviluppati diversi strumenti di imaging non-invasivi, consentendo di ottenere immagini dell'interno del corpo umano mentre il paziente è ancora in vita. Nel contesto neurologico, sistemi di imaging come TAC, RM, SPECT e PET permettono di ricavare biomarcatori utili a distinguere quantitativamente soggetti sani da pazienti con malattie neurologiche, valutare lo stato di avanzamento di una malattia in un paziente, valutare l'efficacia di un trattamento, esplorare le cause della malattia.
Nel presente lavoro si presentano i sistemi di acquisione di immagini RM e PET fin dalle fondamenta, partendo dai metodi di ricostruzione dell'immagine dai dati grezzi, fino allo stato dell'arte dei metodi di post-processing per il calcolo dei biomarcatori più diffusi.
Dopo tale introduzione saranno presentati tre lavori originali di imaging PET/MRI, con una particolare attenzione ai metodi. Questi tre lavori riguardano pazienti con Sclerosi Multipla, Morbo di Alzheimer e Tumori Cerebrali.

Table of Contents

Introduction

> The preface is that part of a book which is written last, placed first, and read least. As I approach my concluding task I am moved to reflect why a preface should be written at all. This question, if followed into all the intricacies of which it holds potentiality, should apparently result in a composition new in literature, a Preface to the Preface.
>
> Alfred J. Lotka, *Elements of Physical Biology*

A modern neurological study aims to relate several biomarkers from different sources in order to explain the illness evolution, improve prognostic accuracy and optimize the treatment. A research group can have at disposal clinical, imaging, neuropsychological, liquor biomarkers, which have shown several interesting relations with other kind of biomarkers.

Neuroimaging offers a fecund and interesting source of biomarkers. Since at present time images of the brain can be obtained in a non-invasive way, some measurements of both morphological and functional features of the brain can be taken *in vivo*. Since morphological and functional images are both needed in Neuroimaging studies [1], the past 5 years of technological development have seen the rise of hybrid systems.

The focus of this document is on the methods for calculate biomarkers from neuroimages data source as Magnetic Resonance Imaging (MRI) and PET/MRI (hybrid between PET and MRI), with some application of these methods being presented as neurological studies. PET/MRI is a recent imaging system able to acquire MRI and PET images at the same time, allowing the researcher to obtain a perfectly matched PET and MRI couple of images, thus reducing significantly the biases from movement and the total scanning time.

Computing biomarkers from Neuroimaging sources can be very time-consuming, also because an increasing number of images can be available from a single patient.

For instance, a study involving three 3D (no more than $1 \times 1 \times 1$ mm^3 of resolution) and two 2D MRI sequences and a 3D dynamic brain PET of 50 patients occupy more than 2Tb of disk space, which can be considered as a Big Data problem [2].
Hence there is need of improving the speed of the algorithms for biomarker extraction without loss of accuracy whenever it is possible. Furthermore, the reliability of the method is important to avoid the wrong conclusions, as remarked by recents works [3]. Since the methods and the pipelines used in neurological studies are a constant work-in-progress, in this work current state-of-the-art and some personal contributions will be presented.

The document is structured as follows: the first Chapter contains an overview on Multiple Sclerosis (MS) and other neurological diseases. In the second and third Chapter MRI and PET will be introduced from a physical/mathematical point of view. The concepts introduced in these two Chapters will be useful to understand the most important algorithms used in Neuroimaging, presented in the fourth Chapter.

At last, Chapters 5, 6 and 7 contains the personal contribution of this work, which can be summarized as a reliable method (and some variants) for PET/MRI biomarker extraction and its application to Multiple Sclerosis (MS, CHapter 5), Alzheimer's Disease (AD, Chapter 6) and Brain Tumors (Chapter 7).
The method relies upon a 2-phase PET/MRI (early and latter phase) which has been projected for two main purposes:

- First, to mimic and discern the behavior of the tracers used in PET, whose signal is usually growing quickly in the early phase of uptake and almost constant (all signals are corrected for decay of course) in the latter phase.

- Second, to achieve an exam that the patient could tolerate more easily. In fact two sessions of 20 minutes circa with an intermediate rest time of 20 min is sufficient to obtain a signal as significant as the full 1 hour exam for the biomarker computation purposes.

This approach leads to a postprocessing pipeline that can be applied, after proper adjustments, both to static PET images as in Chapter 6 and to dynamical PET series as in Chapters 5 and 7. Other choices different from the state-of-the-art pipelines will be explained in detail right after their introduction in Chapters 5, 6 and 7.

The statistical results of the clinical studies in the last three Chapters will also be

presented, along with the discussion of such results, attempting to recover a meaningful and clinically-consistent interpretation of the data.

Bibliography

[1] CJ Aine, *A conceptual overview and critique of functional neuroimaging techniques in humans: I. MRI/FMRI and PET*, Critical reviews in neurobiology, 1994

[2] M Chen, S Mao, Y Liu, *Big data: a survey*, Mobile Networks and Applications, Springer 2014

[3] A Eklund, TE Nichols, H Knutsson, *Cluster failure: Why fMRI inferences for spatial extent have inflated false-positive rates*, Proceedings of the National Academy of Sciences of the USA, 2016

Chapter 1

Multiple Sclerosis and other neurological diseases

> "This is Knobloch reporting that a terrible mistake has been made. You were accidentally assigned to an experimental canister. The canister you've been occupying is actually a giant sensor. It records your heartbeat, your electrical brain activity, your oxygen intake, your eye movements, your cerebral blood flow and countless other functions that can be studied on EEG and similar tracings. Say "I read" if you read what I'm saying."
> "I read."
> "Nobody's supposed to occupy that canister except on an experimental basis. You were put in there accidentally. The room is extensively shielded from outside interference. The walls, the floors and all the furniture are equipped with extremely superfine sensing devices. The only way you could avoid being traced would be to suspend yourself in midair. Literally everything you've done has been recorded, measured and studied. Except we didn't know until now that the tracings we've been getting belong to you."
> "I read but do not understand."
>
> Don DeLillo, *Ratner's Star, 1976*

Neurological diseases, or neurological disorders are the medical conditions involving the human brain. This chapter contains a brief introduction to some neurological diseases as Multiple Sclerosis (MS, Section 1), Alzheimer's Disease (AD, Section 2) and Brain Tumors in Section 3. In these Sections the most important features of each disease are explained.

1.1 Multiple Sclerosis

Multiple Sclerosis is a inflammatory, chronic, neurodegenerative disease involving both White Matter (WM) an Grey Matter (GM) of the Central Nervous System (CNS). It represents the first cause of non-traumatic disability in the young adult[4], and in Italy the prevalence is estimated around 140 cases over 100 000 inhabitants[15].
The exact causes and underlying immunopathogenetic mechanisms of the short and long-term damages in MS are not yet fully known. However there are several evidences of genetical and environmental factors contributing to the loss of tolerance to myelin antigenes and to the development of an autoimmune response to the CNS[7].
MS is characterized by the presence and appearance of plaques of inflammation[1].
The inflammation is believed to be caused by an apparently random activation of microglia cells (part of the CNS immune system) and it causes demyelinization and by consequence neurodegeneration, which is faster in MS patients than in normal aging healthy subjects. MS has different stages and clinical subtypes[4]: Clinically Isolated Syndrome (CIS) are patients with the first symptoms and MRI evidences, but not or not yet enough proves to get MS diagnosis. Relapse-Remitting MS (RRMS) are patients with episodes of clinical and cognitive relapse, followed by a phase of reprise. Primary and Secondary Progressive MS (PPMS, SPMS) are patients with no signs of relapse and remit, but a continuous and constant worsening from clinical and cognitive points of view. PPMS develop such characteristic from the beginning of the illness, while SPMS after a period of relapse and remit.

1.1.1 WM and GM damage in MRI

It is possible to detect areas afflicted with demyelinization with specific sequences of MRI imaging. Such areas are also referred as **lesions**.
The most used sequence for detecting WM lesion is called Fluid Attenuated Inversion Recovery (FLAIR), a T2-weighted sequence who aims to suppress the signal of CSF. In such sequence most of MS WM lesions appear as hyper-intense signal[1]. About 30% of FLAIR detectable lesions appear as hypo-intense in T1-weighted images[17]. Such lesions are characterized by loss of tissue, and are called black holes[2].
MS is still considered as a prevalently WM disease: diagnostic criteria currently in use require evidences of WM lesions. However recent publications have shown the importance of GM inflammatory lesions in the accumulation of clinical and cognitive disability. Signs of cortical relapses have been found in some patients at early stage[22], suggesting that the GM involvement in inflammation might closely follow or precede WM inflammation process.

[1] from which the French name *Sclerose a Plaques* and the former Italian denomination *Sclerosi a Placche*.

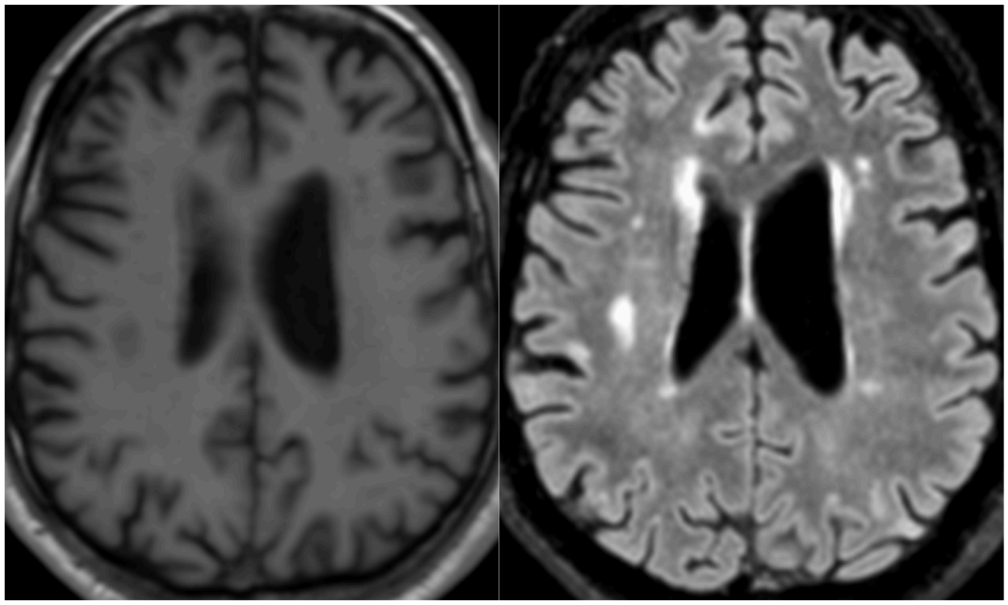

Figure 1.1: T1 (left) and FLAIR (right) sequences of the same slices. Note that only a part of FLAIR hyperintense lesions are black holes in T1.

GML are harder to detect *in vivo*, probably because of the small dimensions, a signal intensity similar to GM, and partial volume effect. By comparing histopathological and neuroradiological images it is evident that MRI-detectable GML are only a small part of the lesions observed in histology[13].
During the last ten years new MRI sequences for detecting GML have been developed. Double Inversion Recovery (DIR), a T2-weighted sequence with double inversion to suppress both CSF and WM signals, has shown more sensibility and specificity than FLAIR in detecting GML[9]. More recently, Phase Sensitive Inversion Recovery (PSIR), a T1-weighted sequence with high GM/WM contrast, has been proved to detect more GML than DIR and a better delineation[14]. PSIR has also shown at least one cortical lesion not only in every MS patient but also in CIS patients[8].

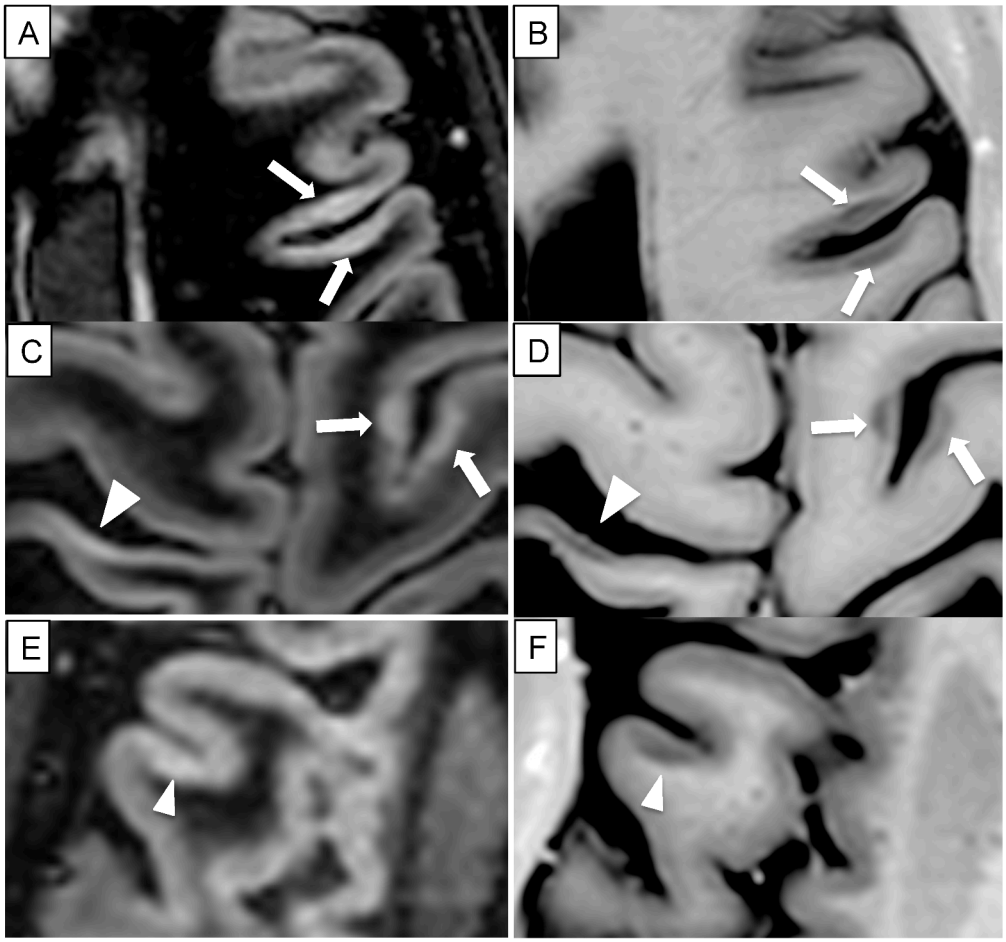

Figure 1.2: DIR (left) and PSIR (right) sequences of the same slices. With full arrows are indicated the GML detected by both sequences, while with arrow heads are indicated lesions detected only by PSIR sequence.

1.2 Alzheimer's Disease

Alzheimer's Disease (AD) is the most common progressive neurodegenerative illness in elder age. The annual incidence goes from 1% between 60 and 70 years of age to 7% after 85 [15]. First symptoms of AD are generally loss of memory and attention, and the most important risk factors are age, familiarity and gender [16]. Although the exact pathogenesis remains unclear, it has been shown that a fundamental role is played by the brain accumulation of beta-amyloid, excessively produced in the brain of AD patients [23].
Amyloid accumulation can be observed long time before the apparition of symptoms [11]. However at present day drugs aimed to reduce amyloid storing have given

no sign of patient improvement [24].
The most popular hypothesis [11] about the illness process refers that that amyloid accumulation *leads to a cascade characterized by abnormal tau aggregation, synaptic dysfunction, cell death, and brain shrinkage.*

1.3 Brain Tumors

In Europe and in the US the incidence of primitive cerebral tumors is up to 10 over 100 000 people each year [26], with peak of prevalence between 0 and 4 years and 65 and 79 years [12]. Gliomas are about 40% of cerebral tumors and develops in the glia cells, support cells for CNS. Tumors are rated in grades according to malignity and spread speed. Tumors of grade III and IV, for whom the survival time goes from 13 to 36 months, are called **high grade**.
Treatment of brain tumor includes:

- **neurosurgery**, aimed to physically remove the tumor mass. Complete removal of tumor tissue through surgery is possible only in few cases, so the goal of such intervention is mostly to obtain an histological diagnosis and to reduce the tumor mass and its eventual pressure.
- **radiotherapy**, aimed to reduce the tumor mass with a targeted exposure. Radiotherapy can lead to cognitive decline, because it is impossible in practice to hit only the areas of brain affected by the tumor.
- **chemotherapy**, which has been shown to increase the survival time by 2.5 months.

All these steps strongly depend on imaging techniques to identify the tumor areas and the post-surgery relapse. The treatment can achieve the goal of some months of survival in high grade tumors, the complete removal of the tumor in low grades.

Bibliography

[1] GJ Barker et al., *3D fast flair: a CSF-nulled 3D fast spin-echo pulse sequence*. Magn. Reson. Imaging, 1998.

[2] F Barkhof, JC McGowan, et al., *Hypointense multiple sclerosis lesions on T1-weighted spin echo magnetic resonance images: their contribution in understanding multiple sclerosis evolution*, J. Neurol. Neurosurg. 1998.

[3] M Calabrese, M Atzori, et al. *Cortical atrophy is relevant in multiple sclerosis at clinical onset* J Neurol, 2007.

[4] M Calabrese, P Gallo, *Magnetic resonance evidence of cortical onset of multiple sclerosis*, Mult Scler 2009.

[5] M Calabrese, I Mattisi, et al., *Magnetic resonance evidence of cerebellar cortical pathology in multiple sclerosis*, J Neurol Neurosurg Psychiatry, 2010.

[6] M Calabrese, F Rinaldi, et al., *The predictive value of gray matter atrophy in clinically isolated syndromes*, Neurology 2011.

[7] CA Dendrou, L Fugger, MA Friese, *Immunopathology of multiple sclerosis*. Nat. Rev. Immunol, 2015.

[8] A Favaretto, D Poggiali, A Lazzarotto, G Rolma, F Causin, P Gallo, *The Parallel Analysis of Phase Sensitive Inversion Recovery (PSIR) and Double Inversion Recovery (DIR) Images Significantly Improves the Detection of Cortical Lesions in Multiple Sclerosis (MS) since Clinical Onset*, PLoS One, 2015.

[9] JJG Geurts et al., *Cortical lesions in multiple sclerosis: combined postmortem MR imaging and histopathology*, Am. J. Neuroradiol, 2005.

[10] RG Henry, et al., *Regional grey matter atrophy in clinically isolated syndromes at presentation*, J Neurol Neurosurg Psychiatry, 2008.

[11] CRJ Jack, DS Knopman, et al., *Hypothetical model of dynamic biomarkers of the Alzheimer's pathological cascade.*, Lancet Neurol. 2010

[12] P Kleihues, M Kiessling, BW Scheithauer, *The new WHO classification of brain tumours*, Brain Pathol, 1987.

[13] CF Lucchinetti, et al., *Inflammatory cortical demyelination in early multiple sclerosis*, N. Engl. J. Med, 2011.

[14] R Magliozzi, et al., *Meningeal B-cell follicles in secondary progressive multiple sclerosis associate with early onset of disease and severe cortical pathology*, Brain 2007.

[15] R Mayeux, *Epidemiology of neurodegeneration*, Annu Rev Neurosci, 2003.

[16] Mayeux R., *Early alzheimer's disease*, N Engl J Med, 2010.

[17] DH Miller, RI Grossman, et al., *The role of magnetic resonance techniques in understanding and managing multiple sclerosis*, Brain 1998.

[18] K Morgen, G Sammer, et al., *Evidence for a direct association between cortical atrophy and cognitive impairment in relapsing-remitting MS*, Neuroimage, 2006.

[19] F Mori, GC Nicoletti CG, et al., *Growth factors and synaptic plasticity in relapsing-remitting multiple sclerosis*, Neuromolecular Med, 2014.

[20] JH Noseworthy, C Lucchinetti, et al., *Multiple sclerosis*, N. Engl. J. Med., 2000.

[21] M Pugliatti, et al., *The epidemiology of multiple sclerosis in Europe*, Eur. J. Neurol., 2006.

[22] M Puthenparampil, D Poggiali, F Causin, G Rolma, F Rinaldi, P Perini, P Gallo, *Cortical relapses in multiple sclerosis*, Multiple Sclerosis Journal, 2015.

[23] DJ Selkoe, *Physiological production of the beta-amyloid protein and the mechanism of alzheimer's disease*, Trends Neurosci, 1993.

[24] JD Smith, JA Levin-Allerhand, *Potential use of estrogen-like drugs for the prevention of alzheimer's disease*, J Mol Neurosci, 2003.

[25] M Vercellino, F Plano, B Votta, et al., *Grey matter pathology in multiple sclerosis*, J Neuropathol Exp Neurol, 2005.

[26] M Wrensch, Y Minn, T Chew, M Bondy, MS Berger, *Epidemiology of primary brain tumors: Current concepts and review of the literature*, Neuro Oncol, 2002.

Chapter 2

Magnetic Resonance Imaging

> "Interesting you should call just now. Because I'm clipping my toenails into a wastebasket several meters away."
> "Jesus, you know how I hate the sound of nail clippers."
> "Except I'm shooting seventy-plus percent. The little fragments of clipping. It's uncanny. I keep wanting to go out in the hall and get somebody in here to see it. But I don't want to break the spell."
> "The fragile magic-spell feel of those intervals where it feels you just can't miss."
> "It's definitely one of those can't-miss intervals. It's just like that magical feeling on those rare days out there playing. Playing out of your head, de-Lint calls it. Loach calls it The Zone."
>
> David Foster Wallace, *Infinite Jest*

In this chapter Magnetic Resonance Imaging (MRI) is introduced from a physical mathematical point of view. This introduction can be helpful to the reader to understand how the MRI images are generated and why different MRI scans look so different one to another. In fact MRI, oppositely to Computed Tomography (CT) is a multiparametric imaging system. Tuning the parameters differently brings different images with different features, which can be useful to detect different issues in the tissue.

2.1 What is MRI

Magnetic Resonance Imaging (MRI), elderly known as Nuclear Magnetic Resonance (nMR[1]) is an *in vivo* medical imaging system that uses the resonance property of

[1] the n has been removed to underline the complete safety of this kind of exam.

physical objects under properly designed magnetic fields to generate image representing the inside of the object [1, 2, 3, 4]. This exam is non-invasive and much secure compared to the analog X-ray tomography. In fact the electromagnetic rays in use have a maximum frequency of about 10^5Hz (which is in the order of radio waves), which is much less than the X-ray frequency, about 10^{16}Hz. A higher frequency means a shorter wavelength, a greater energy and by consequence a greater mutagen power. RMI is said to be "safe" as the probability of a genetic mutation of the RNA a cell is low. To make more safe the using of X, γ and β rays the time of exposition has to be reduced.

2.2 A Physical introduction

2.2.1 The spin

The nucleus of an atom has a property called **spin**. This means that an atom can be considered as a spinning wheel. This property leads also to an electromagnetic effect: each nucleus generates a small magnetic field. Thus nuclei can be thought as magnets with North and South poles on the rotation axes of the nuclei.
For our purpose the nucleus of hydrogen (H) will be considered, because it has an odd number of protons and so the magnetic moment is not null and also because it is very common.
So a proton p has an intrinsic angular momentum J_p and a magnetic momentum μ_p. There exists a direct proportion between these two quantities

$$\mu_p = \gamma_p J_p$$

where γ_p is a constant called *gyro-magnetic ratio* and it is related to the kind of atom in examination. For instance the hydrogen has a ratio equal to $\gamma_H \cong 2.68\, T^{-1} s^{-1}$. To be more precise the gyro-magnetic ratio depends on the chemical bound of the atom

$$\gamma_p = (1-\sigma)\gamma$$

where the constant $\sigma \in [10^{-6}, 10^{-4}]$ is called *chemical shift*.
Now if a stationary and uniform magnetic field $\boldsymbol{B_0}$ is turned on, the quantum mechanic expected value of the intrinsic angular momentum will satisfy the law

$$\frac{d < J_p >}{dt} = < \mu_p > \times \boldsymbol{B_0}$$

so, given the proportion obtained,

$$\frac{d < \mu_p >}{dt} = \gamma < \mu_p > \times \boldsymbol{B_0}.$$

Since it is impossible to measure the momentum of every single atom, the (total) magnetic momentum $\boldsymbol{M}$, defined as

$$\boldsymbol{M} = \sum_p \mu_p$$

can be measured instead. This allows to formulate the differential equation

$$\dot{\boldsymbol{M}} = \gamma \boldsymbol{M} \times \boldsymbol{B_0} \tag{2.1}$$

which will be fundamental for our purposes. Even if the nuclei are under a quantum

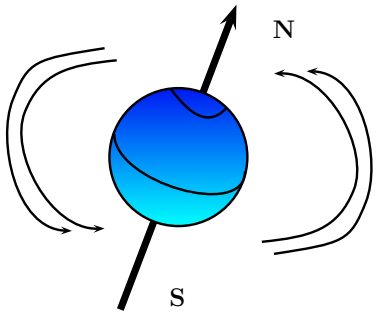

Figure 2.1: A nucleus of hydrogen can be seen as a magnetic wheel.

effect, a classical approach will be more feasible and will not lead to great errors.

2.2.2 Magnetic fields and relaxation

In absence of an external magnetic field the nuclei arrange themselves randomly and their momentums mutually annul, so $\boldsymbol{M} = 0$. Since the magnetic field of the Earth is weak (from 2 to $7 \cdot 10^{-5}$ T), a normal body has a magnetic momentum $\boldsymbol{M} \approx 0$.
Otherwise, if a stationary magnetic field is turned on along the z-axis

$$\boldsymbol{B_0} = (0, 0, B_0),$$

the nuclei will show a sort of *herd mentality*. In fact their rotation axes arrange themselves parallel to the axis z. Some of them align themselves with the same verse of $\boldsymbol{B_0}$ (low energy), and some others will take the opposite direction (high energy). As will be described in the next section, the most part of the nuclei will arrange in a low energy position.

A more accurate description of the motion reveals that the axes has a **precession** along the direction of the external field at the same frequency ω_0, called the **Larmor frequency**, but with different phases.
The precession tends to the equilibrium $(0, 0, M_{eq})$ exponentially, with a recovery time

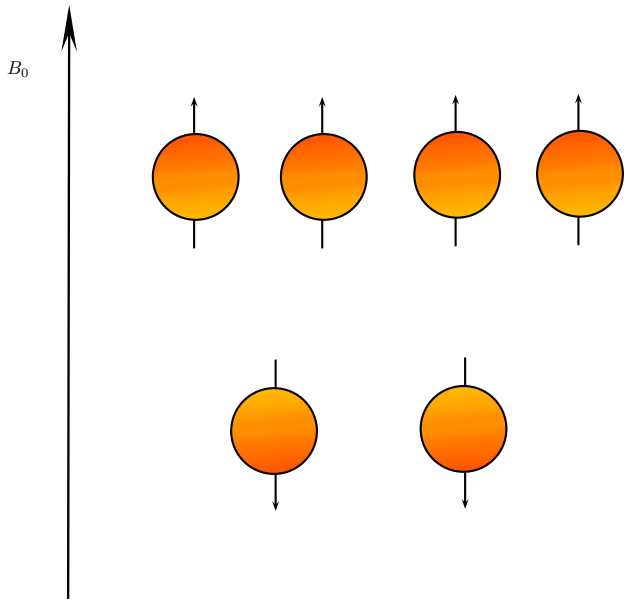

Figure 2.2: Herd mentality of the nuclei under a magnetic field.

T_1 (spin-lattice) along the axis z, and with a loss time T_2 (spin-spin) along the plane xy. These two times are different because of the different phase of the nuclei.
The parameters T_1 and T_2 depends from the chemical bound of the Hydrogen molecules, then from the tissue.
The main issue is that the precession is not visible for the total momentum because the convergence to the equilibrium is too fast.

2.2.3 Attempt for seeing the relaxation

The disposition of the nuclei in the verse of the magnetic field causes the precession motion to be difficultly measurable. To make the precession visible the alignment to the axis of the nuclei has to be tuned in some way. According to the *Boltzmann factor*, the probability that a nucleus arranges himself along the z-axis is equal to the negative exponential of the ratio between magnetic and thermal energy,

$$P(E_i) = \exp\left(-\frac{E_{magn}}{E_{therm}}\right) = \exp\left(-\frac{\gamma B_0 \hbar}{k_b T_K}\right)$$

where $\hbar \cong 1.05 \cdot 10^{-34}\, Js$ is the normalized Plank constant, $k_b \cong 1.38 \cdot 10^{-23}\, JK^{-1}$ is the Boltzmann constant and T_K is the absolute temperature in Kelvin degrees.

Let us calculate this value for a typical MRI experiment, $B_0 = 1T$, $T = 300K$.

$$P(E_i) \cong \exp\left(-\frac{3\,s^{-1}T^{-1}\cdot 1\,T\cdot 10^{-34}\,Js}{1\cdot 10^{-23}\,JK^{-1}\cdot 3\cdot 10^{2}K}\right) = \exp\left(-10^{-13}\right)$$

from the first order Taylor approximation it follows

$$P(E_i) \cong 1 - 10^{-13}.$$

This means that only one atom over 10^{13} chooses a high energy position, and the magnetic momentum tends quickly to the z-axis.
From the Boltzmann factor comes an idea to make more measurable the precession: decreasing the room temperature or increasing the external magnetic field.
For having a visible change two parameters must change to values that are physically unacceptable for an *in vivo* acquisition. In conclusion another way to make the precession measurable has to be found.

2.2.4 RF pulse and resonance

To move down the magnetic momentum the engineers had to resort to a *Radio-frequency pulse* (RF-pulse), a second magnetic field $\boldsymbol{B_1}$ of a minor intensity than the static field and rotating along the plane xy at *exactly* the Larmor frequency ω_0. In this way a physical phenomenon will occur, the **magnetic resonance**. In fact a huge number of nuclei will gain energy and the magnetic momentum $\boldsymbol{M}$ will separate from the z-axis.
Moreover, with the RF field turned on the phase of the precession will align, while when the RF field is turned off there will be "dephasing".

2.3 A Toy-model: the Bloch equations

To see mathematically phenomenons described in the previous section, toy-model is needed, a set of mathematical equations that describes the motion of the aggregate magnetic momentum $\boldsymbol{M} = (M_x, M_y, M_z)$. So let us consider the equation (2.1The spinequation.2.2.1) applied to an external field $\boldsymbol{B}$ and study the solution of this equation for several external fields.

2.3.1 Static field

Let us consider the case that only the static field along the axis z is on, $\boldsymbol{B} = (0, 0, B_0)$. If a relaxation term is added to describe the polarization appears along the axis z (T_1),

and the decay along the xy-plane (T_2).
This leads to formulate the **Bloch equation**

$$\dot{\boldsymbol{M}} = \gamma \boldsymbol{M} \times \boldsymbol{B} - \left(\frac{M_x}{T_2}, \frac{M_y}{T2}, \frac{M_z - M_{eq}}{T_1} \right) \tag{Bloch-1}$$

rewriting this equation component-wise

$$\begin{cases} \dot{M}_x &= M_y B_0 - \frac{M_x}{T_2} \\ \dot{M}_y &= M_x B_0 - \frac{M_y}{T_2} \\ \dot{M}_z &= -\frac{M_z - M_{eq}}{T_1} \end{cases} \tag{2.2}$$

The solution to this ODE is

$$\begin{cases} M_x &= e^{-t/T_2}(M_{x,0}\cos\omega_0 t - M_{y,0}\sin\omega_0 t) \\ M_y &= e^{-t/T_2}(M_{x,0}\sin\omega_0 t + M_{y,0}\cos\omega_0 t) \\ M_z &= M_{z,0}\, e^{-t/T_1} + M_{eq}(1 - e^{-t/T_1}) \end{cases} \tag{2.3}$$

where $\omega_0 = -\gamma B_0$ is the Larmor frequency. This is clearly a precession along the $z-$axis at the Larmor frequency, and the solution tends to the equilibrium $(0,0,M_{eq})$ in a exponential way, so the precession is very hard to see experimentally.

2.3.2 RF pulse

Turning on a RF pulse, the magnetic field rotates with angular speed ω in the plane xy, with equations $\boldsymbol{B} = (B_1\cos\omega t, B_1\sin\omega t, B_0)$. The relaxation terms are ignored, since the RF-pulse is on, resulting

$$\dot{\boldsymbol{M}} = \gamma \boldsymbol{M} \times \boldsymbol{B} \tag{2.4}$$

again, rewriting the equation element-by-element,

$$\begin{cases} \dot{M}_x &= \gamma\left(M_y B_0 - M_z B_1 \sin\omega t\right) \\ \dot{M}_y &= \gamma\left(M_z B_1 \cos\omega t - M_x B_0\right) \\ \dot{M}_z &= \gamma\left(M_x B_1 \sin\omega t - M_z B_1 \cos\omega t\right) \end{cases} \tag{2.5}$$

Now, for simplicity, the system will be studied in a reference frame rotating along the axis z like the RF pulse.

$$\begin{cases} \boldsymbol{e1} &= (\cos\omega t, & \sin\omega t, & 0) \\ \boldsymbol{e2} &= (-\sin\omega t, & \cos\omega t, & 0) \\ \boldsymbol{e3} &= (0, & 0, & 1) \end{cases} \tag{2.6}$$

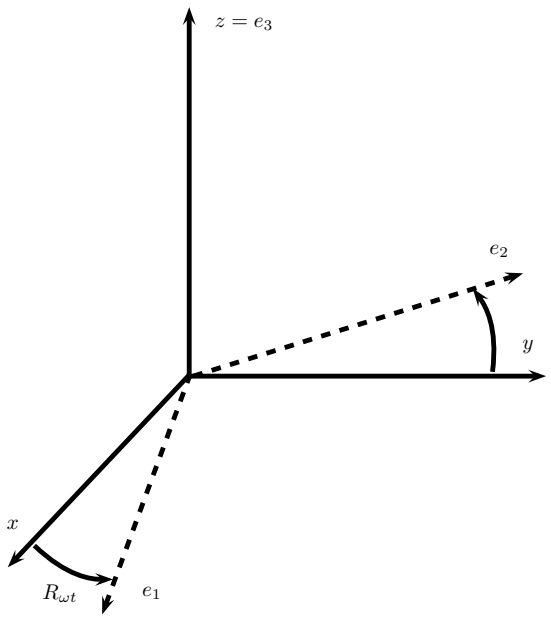

Figure 2.3: The rotating non-inertial frame $\{e_1, e_2, e_3\}$

Considering the functions

$$\begin{pmatrix} u(t) \\ v(t) \end{pmatrix} = R_{\omega t} \begin{pmatrix} M_x(t) \\ M_y(t) \end{pmatrix} \tag{2.7}$$

where $R_{\omega t}$ is the matrix of rotation of angle ωt.
Substituting the functions (2.7RF pulseequation.2.3.7) in the system (2.5RF pulseequation.2.3.5) it is possible to obtain

$$\begin{cases} \dot{u} &= \left(\gamma B_0 + \omega\right) v \\ \dot{v} &= -\left(\gamma B_0 + \omega\right) u + \gamma B_1 M_z \\ \dot{M}_z &= -\gamma B_1 v \end{cases} \tag{2.8}$$

Now, if the angular speed of the RF pulse is exactly the Larmor frequency $\omega = \omega_0 = -\gamma B_0$ the system is simplified and a second version of Bloch equation can be obtained

$$\begin{cases} \dot{u} &= 0 \\ \dot{v} &= \gamma B_1 M_z \\ \dot{M}_z &= -\gamma B_1 v \end{cases} \tag{Bloch-2}$$

This means that the system is affected by resonance, since the aggregate momentum tends to move down from the equilibrium position. This result is known as **Larmor**

Theorem. The solution of this equation is simple:

$$\begin{cases} u &= u_0 \\ v &= v_0 \cos\omega_1 t - M_{z,0} \sin\omega_1 t \\ M_z &= v_0 \sin\omega_1 t + M_{z,0} \cos\omega_1 t \end{cases} \tag{2.9}$$

where, as before $\omega_1 = -\gamma B_1$.
The motion in inertial reference frame is the composition of two circular uniform

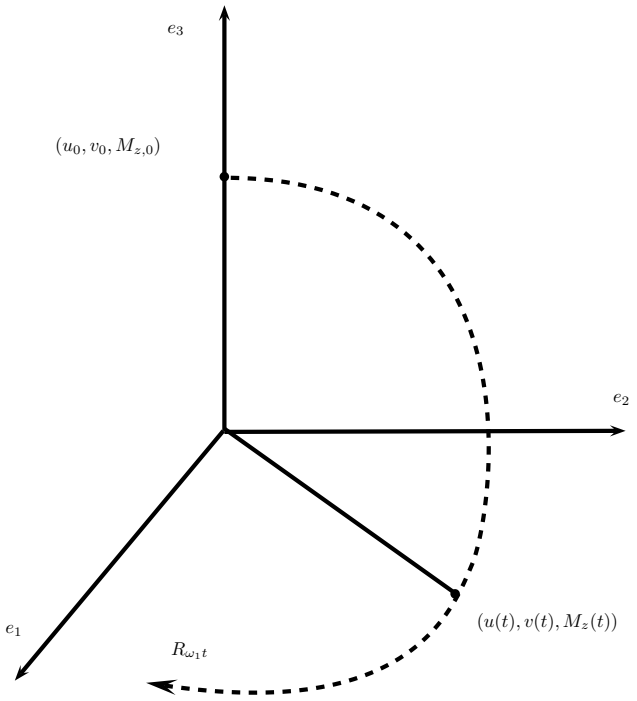

Figure 2.4: The solution of the second Bloch equation in the non-inertial reference frame.

motions in orthogonal directions, which means that the motion in analysis is a uniform helical motion over a sphere.

2.3.3 Gradient pulse

For reasons that soon will be clear, sometimes in addiction to the RF pulse **gradient pulse**, another magnetic field along z it is also needed. This pulse has the form

$$\boldsymbol{B_G} = (0, 0, B_g) = (0, 0, G \cdot x)$$

where, for instance, G is a constant vector of $\mathbb{R}^3$. Now, considering a field $B_0 + B_g$ instead of B_0, the Eq. (Bloch-2RF pulseAMS.18) becomes

$$\begin{cases} \dot{u} &= \gamma B_g v \\ \dot{v} &= -\gamma B_g v + \gamma B_1 M_z \\ \dot{M}_z &= -\gamma B_1 v \end{cases} \tag{2.10}$$

Since $B_1 \ll B_0, B_g$, the term B_1 is negligible and thus it is possible to write the third Bloch equation:

$$\begin{cases} \dot{u} &= \gamma B_g v \\ \dot{v} &= -\gamma B_g v \\ \dot{M}_z &= 0 \end{cases} \tag{Bloch-3}$$

The solution to this ODE is similar to the previous

$$\begin{cases} u &= u_0 \cos \omega_g t - v_0 \sin \omega_g t \\ v &= u_0 \sin \omega_g t + v_0 \cos \omega_g t \\ M_z &= M_{z,0} \end{cases} \tag{2.11}$$

where, as one can guess, $\omega_g = -\gamma B_g$.

2.4 Pulse sequences

As can be seen from (2.9RF pulseequation.2.3.9), an RF pulse has the effect to flip the vector $\boldsymbol{M}$ from the axis z of an angle $\theta = \omega_1 \tau$ after a time τ. Thus the following pulses can be applied:

- a general θ-**pulse**: $\tau = \frac{\theta}{\omega_1}$
- a $\frac{\pi}{2}$-**pulse**: $\tau_1 = \frac{\pi}{2\omega_1}$.
  After this pulse the aggregate magnetic momentum is
  $$\boldsymbol{M}(\tau_1) = (u_0, M_{z,0}, v_0)$$
- a π-**pulse**: $\tau_2 = \frac{\pi}{\omega_1}$.
  After this pulse the aggregate magnetic momentum is
  $$\boldsymbol{M}(\tau_2) = (u_0, -v_0, -M_{z,0})$$

Playing with pulses gets more informations about the precession. The following sequences are the most popular ones:

1. inversion recovery
2. saturation recovery
3. spin echo

2.4.1 Inversion recovery

Inversion recovery: after applying a π-pulse, and a waiting time of τ, another $\frac{\pi}{2}$-pulse is applied and M is measured. Waiting for the system to get back to the equilibrium of (2.3Static fieldequation.2.3.3) and repeating several times and for several values of τ results in an increase of the signal-to-noise ratio. This sequence is shorted as follows

$$\left(\pi - \tau - \frac{\pi}{2} - AT - t_\infty\right)_n$$

where AT stands for acquisition time, and t_∞ is a long time needed to get back to the equilibrium, usually $t_\infty \approx 4T_1$.
From the third component of (2.3Static fieldequation.2.3.3) gives

$$M_z(\tau) - M_{eq} = (M_{z,0} - M_{eq}) \exp(-\frac{\tau}{T_1}).$$

This means that $-1/T_1$ can be computed as the slöpe of $\log(M_z(\tau) - M_{eq})$.

2.4.2 Saturation recovery

Saturation recovery: This sequence is shorted as

$$\left(\frac{\pi}{2} - Hs - \tau - \frac{\pi}{2} - AT - Hs\right)_n$$

Where Hs is a pulse that destroys the homogeneity of the field B_0. After a time τ the magnetization is partially recovered, the pulse flips it on the xy-plane. Again, $-1/T_1$ is computed from the slöpe of $\log(M_z(\tau) - M_{eq})$.

2.4.3 Spin echo

This sequence is shorted as

$$\left(\frac{\pi}{2} - \tau - \pi\right)_n$$

After 2τ the amplitude of the transverse magnetization will be relaxed by a factor

$$\exp(2\tau/T_2)$$

2.4.4 T2*

T2* is the real time constant of loss in the xy-plane, because the field $\boldsymbol{B_0}$ is not really homogeneous. The relation between $T2$ and $T2^*$ is quite simple:

$$\frac{1}{T2^*} = \frac{1}{T2} + \gamma \triangle \boldsymbol{B_0}$$

where $\triangle \boldsymbol{B_0}$ is the maximum variance of $\boldsymbol{B_0}$.
T2* can be used in alternative to T2 to obtain different images.

2.5 K-space and reconstruction

2.5.1 From Bloch equations to imaging

The aim of reconstruction is to create a 2D map of the proton density $\boldsymbol{\rho}(\boldsymbol{x})$ on each slice. For this purpose only the transverse component of $\boldsymbol{M}$ is now considered,

$$M^* = M_x + iM_y$$

In a similar way, the signal received from the coils is

$$s = S_x + iS_y$$

For Faraday's law the magnetic field generated by the body induces an electromotive force to the coils

$$\boldsymbol{S(t)} = \frac{d}{dt}\Phi_\gamma = k\frac{d}{dt}\int_\gamma \rho(\boldsymbol{x})\boldsymbol{M}\,d\boldsymbol{x}$$

with γ a single loop in the coil. Now, considering a tiny slice over the z-axis, the previous formula becomes

$$s(t) = k_1\frac{d}{dt}\int_{\gamma'} \rho(\boldsymbol{z})M^*(\boldsymbol{z})\,dz$$

with $\boldsymbol{z} \in \mathbb{C}^2$.

Applying a $\frac{\pi}{2}$-pulse, then a gradient for the selection of a slice, gives

$$M^* = \exp\left(-\frac{t}{T_2} + i\omega_0 t + i\omega_g t\right)$$

and then

$$s(t) = k_2 \exp\left(-\frac{t}{T_2} + i\omega_0 t\right)\int_{\gamma'} \rho(\boldsymbol{z})\exp(i\omega_g t)\,d\boldsymbol{z}.$$

Remembering that $\omega_g = -\gamma B_g = -\gamma \boldsymbol{G}\cdot\boldsymbol{x}$ and setting

$$G = G_x + iG_y$$

the equation becomes

$$s(t) = k_3 \exp\left(-\frac{t}{T_2} + i\omega_0 t\right)\int_{\gamma'} \rho(\boldsymbol{z})\exp(-it\gamma G\cdot\boldsymbol{z})\,d\boldsymbol{z} \tag{2.12}$$

2.5.2 K-space

Looking at the Eq. (2.12From Bloch equations to imagingequation.2.5.12), it is possible to observe that the signal $s(t)$ can be seen as the 2D Fourier Transform of $k(t)$

$$s(t) \propto \mathscr{F}_2[\rho](k(t))$$

where of course $k(t) = -\frac{t\gamma}{2\pi}G$.
So, storing the values of $\frac{s(t)}{k_3 \exp\left(-\frac{t}{T_2}+i\omega_0 t\right)}$ in a matrix called **K-space** and applying the 2-D IFFT algorithm the slice image is finally reconstructed.

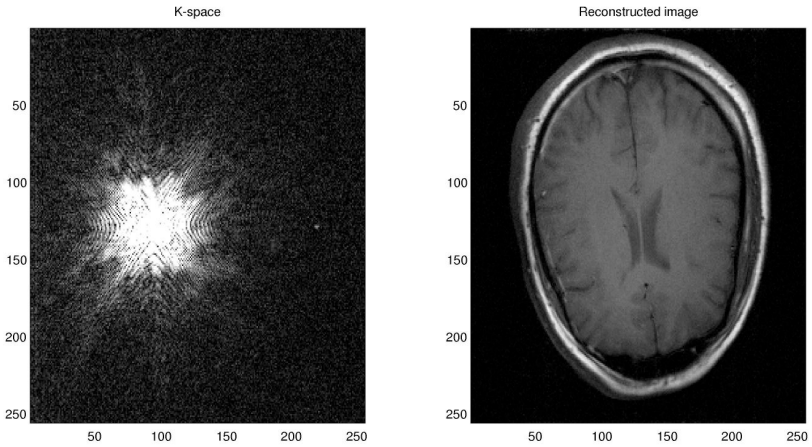

Figure 2.5: An example of K-space and reconstructed image.

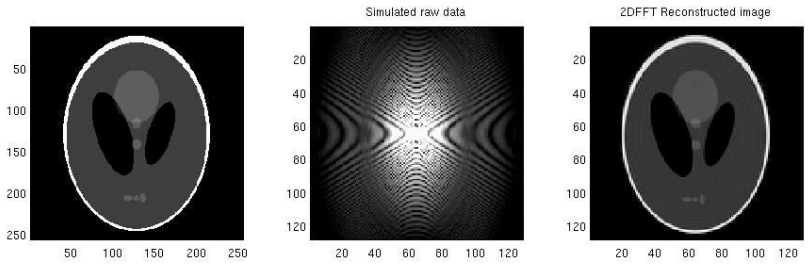

Figure 2.6: A phantom to obtain a simulated K-space.

2.6 TR and TE Parameters

MRI is a **multi-parametric** imaging system: in fact you can play with some parameters to obtain different contrast between the tissues.
Some of these parameters will be introduced in this section.

2.6.1 TR

Repetition Time (TR) is the time interval between the application of a pulse and another.
After TR the longitudinal magnetization of the vector M will be

$$M_z(t) = M_{eq}\left(1 - \mathrm{e}^{-TR/T1}\right)$$

so each FID signal will be proportional to

$$\left(1 - \mathrm{e}^{-TR/T1}\right)$$

This means that the longitudinal magnetization will not reach M_{eq} unless a $TR \gg 4T1$ is set.

2.6.2 TE

TE stands for echo delay time (or time to echo). Instead of making the measurement immediately after the RF pulse (which is impossible in pratice), waiting a short amount of time and then making the measurement will be a better solution.

2.7 Sequences

As stated previously, different images can be acquired from MRI by tuning differently the sequence parameters. Below some of most common MRI sequences and their utility in detecting different features are introduced and explained.

2.7.1 T1-weighted

T1-weighted images are obtained using a **short TR**. Useful in scanning the human brain to see contrast between gray and white matter, 3D T1 images are mostly used for brain tissue segmentation and parcellation since they reveal most of the anatomical informations about the brain.

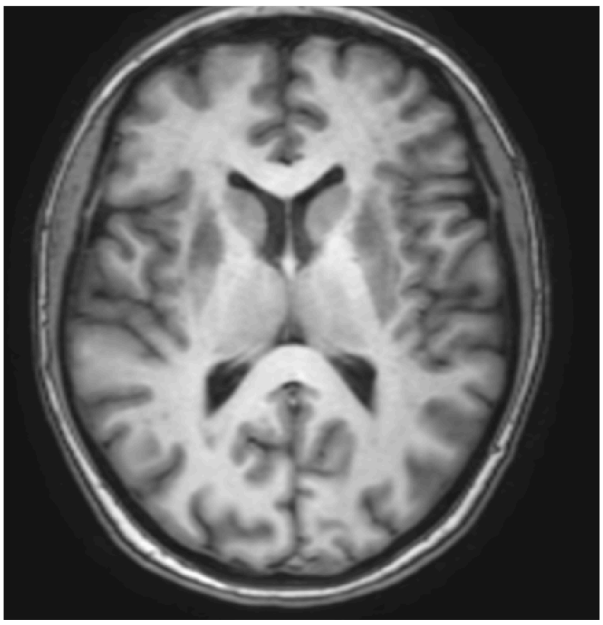

Figure 2.7: An example of axial T1-weighted MRI image of the human brain.

2.7.2 T2-weighted

To get a T2-weighted image **a long TE and a long TR** are applied. This sequence is used to see the contrast between water and fat. From this sequence it is derived the Fluid Attenuated Inversion Recovery (FLAIR), used for the detection of lesions (MS lesions above all) in the white matter of the brain. Another T2-derived sequence is the Double Inversion Recovery (DIR), where a second inversion is applied to the sequence in order to suppress the signal from normal appearing white matter. DIR images have shown to reveal MS lesions in the gray matter.

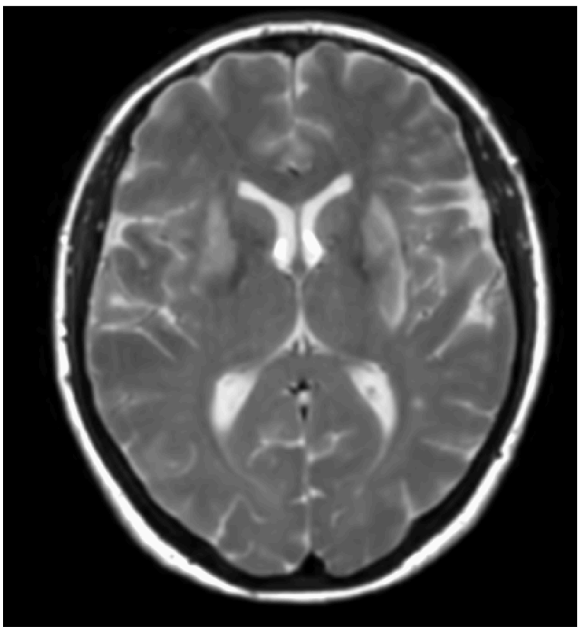

Figure 2.8: An example of axial T2-weighted MRI image of the brain.

2.7.3 Proton density

Using **a short TE and long TR** an image called *Proton Density* or PD is acquired. This sequence is used to minimize the effect of $T1$ or $T2$ times in order to obtain a measure of the hydrogen density in each voxel. The images obtained using PD sequences appear much similar to Computed Tomography (CT) images, but unlike CT does not offer a measure of the attenuation coefficient of the tissue.

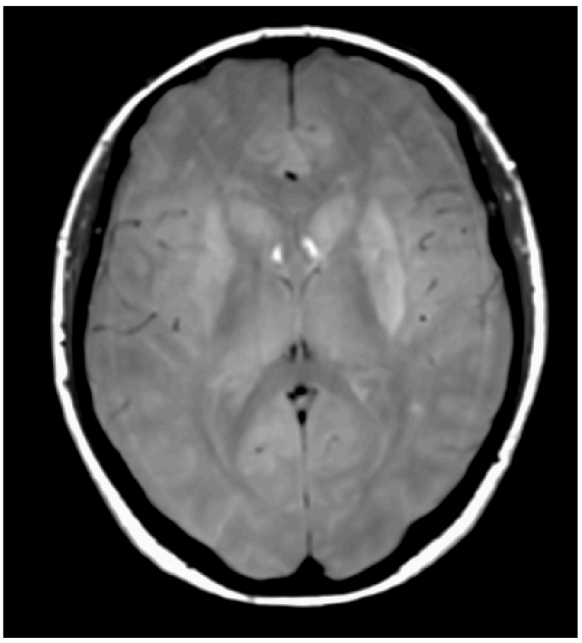

Figure 2.9: An example of axial Proton Density MRI image of the brain.

Bibliography

[1] P Callaghan, *Principles of Nuclear Magnetic Resonance Microscopy*, Oxford University Press 1994.

[2] CL Epstein, *Introduction to the mathematics of Medical Imaging*, Second Edition, Siam, 2008, Ch14.

[3] TG Feeman, *The mathematics of medical imaging: A beginners guide*, Springer, 2010, Ch10.

[4] RH Hashemi, WG Bradley, CJ Lisanti, *MRI, the Basics*, Lippincott Williams & Wilkins, 2010.

Chapter 3

Positron Emission Tomography

> Fenton here was a dyed-in-the-wool paranoid schizophrenic who believed that radioactive fluids were invading his skull and that hugely complex high-tech-type machines had been specially designed and programmed to pursue him without cease [...]. With the aid of cutting-edge Positron-Emission Topography or 'P.E.T.' technology [...], they could scan and study how different parts of poor old Fenton's dysfunctional brain emitted positrons in a whole different topography than your average hale and hearty nondelusional God-fearing Alber-tan's brain, advancing science by injecting test-subject Fenton here with a special blood-brain-barrier-penetrating radioactive dye and then sticking him in the rotating body-sized receptacle of a P.E.T. Scanner
>
> David Foster Wallace, *Infinite Jest*

Positron Emission Tomography shall be introduced in this Chapter, along with some notion of tracer kinetics which will guide the reader to learn about the Sokoloff model and the Patlak plot method. These methods are used for computing the absolute rate of glucose metabolism (aMRGlu.) which will be treated in the next chapters.

3.1 General introduction

3.1.1 What is PET

Positron emission tomography (PET) is a nuclear medical imaging technique that produces an image of functional processes in the body. The PET machine detects pairs

of **gamma rays**, or **positrons** emitted by the annihilation of a tracer (as the ^{18}FdG), introduced into the body [2, 5, 8].

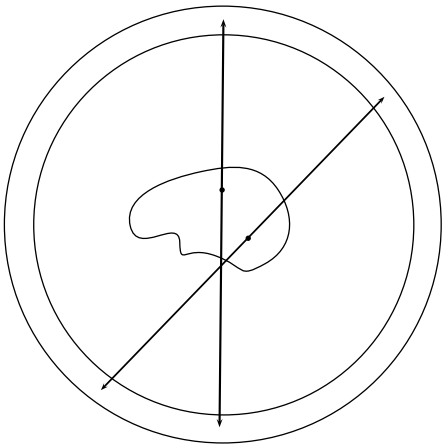

Figure 3.1: Scheme of acquisition for the PET imaging system.

The particularity of PET stands in the possibility to recovering a sequence of images as a **time series**. This allows the researchers to study the evolution of the tracer kinetics.
Since the positrons are emitted two by two, before considering a couple of data as the product of the same annihilation process, the machine filters only the pairs of positrons incoming in the same (small) temporal window $\triangle t$. This allows to reduce the effect of scattering, so the data collected after this filtering is quiet reliable.

3.1.2 Mathematical modeling

The mathematical models for the PET scan will be briefly introduced.
This is the Radon transform used in Computed Tomography (CT) [5, 7]

$$\mathscr{R}f(t,\theta) = \int_{\ell_{t,\theta}} f(\bar{x})\, d\bar{x}$$

where f is the image to reconstruct and $\mathscr{R}f(t,\theta)$ its projections on the plane of acquisition. It is possible to recover the image f, for instance by using the inverse of the Radon transform, the **filtered backprojection** formula

$$f = \frac{1}{2}\mathscr{R}^*\left[\mathscr{F}^{-1}(|\nu|\mathscr{F}(\mathscr{R}f))\right] \tag{3.1}$$

where $\mathscr{F}$ is the Fourier Transform and $\mathscr{R}^*$ is the Backprojection Operator, defined as

$$\mathscr{R}^* g(x,y) = \frac{1}{|S^1|}\int_{S^1} g(\bar{x}\cdot\bar{\theta},\theta)\, d\theta.$$

In case of functional tomography as PET or SPECT, the attenuated Radon transform is used

$$\mathscr{R}_a f(t,\theta) = \int_{\ell_{t,\theta}} \exp\left(-\mathscr{D}a(\bar{x})\right) f(\bar{x})\, d\bar{x}$$

where the divergent beam transform is defined as

$$\mathscr{D}a(\bar{x}) = \int_{\ell^+_{t,\theta}(\bar{x})} a(\bar{y})\, d\bar{y} = \int_0^{+\infty} a(x+s\theta)\, ds\,.$$

In this notation $a(\bar{x})$ is a map of attenuation, obtained by an aligned CT (or MRI-obtained pseudoCT image), or estimated for the target zone of the body (as brain, thorax, legs).

In PET case the coils receive two signals in the opposite direction ℓ^+ and ℓ^-, belonging to the same line ℓ. So in that case the integral of a does not depend on $\bar{x}$, and then the attenuated Radon transform Equation can be rewritten as

$$\widetilde{\mathscr{R}}_a f(t,\theta) = \exp\left(-\mathscr{R}a(t,\theta)\right) \mathscr{R}f(t,\theta)$$

This fact allows to correct the attenuation with ease in case the attenuation map a is known.
Reconstruction can be made simply using filtered backprojection formula after correcting for attenuation with simple multiplication by a factor $\exp\left(-\mathscr{R}a(t,\theta)\right)$.

3.2 Kinetics of the Tracer in PET

In case PET images are axtracted as a temporal sequence of images (or **in list-mode**) it is possible to use them as measures for the identification of a model [2, 3, 4]. This identification can bring information about the whole process.

3.2.1 What are compartment models

A **compartment** model is a type of mathematical model used for describing how materials or energies are transmitted among the compartments of a system. Each compartment is assumed to be a homogeneous entity. Hence a compartment represents, in medical application, a group of organs exchanging material at the same speed one with another.
The kinetics of the material is described by an **ordinary differential equations** system with, as unknown functions, the concentration of the considered material in each compartment.

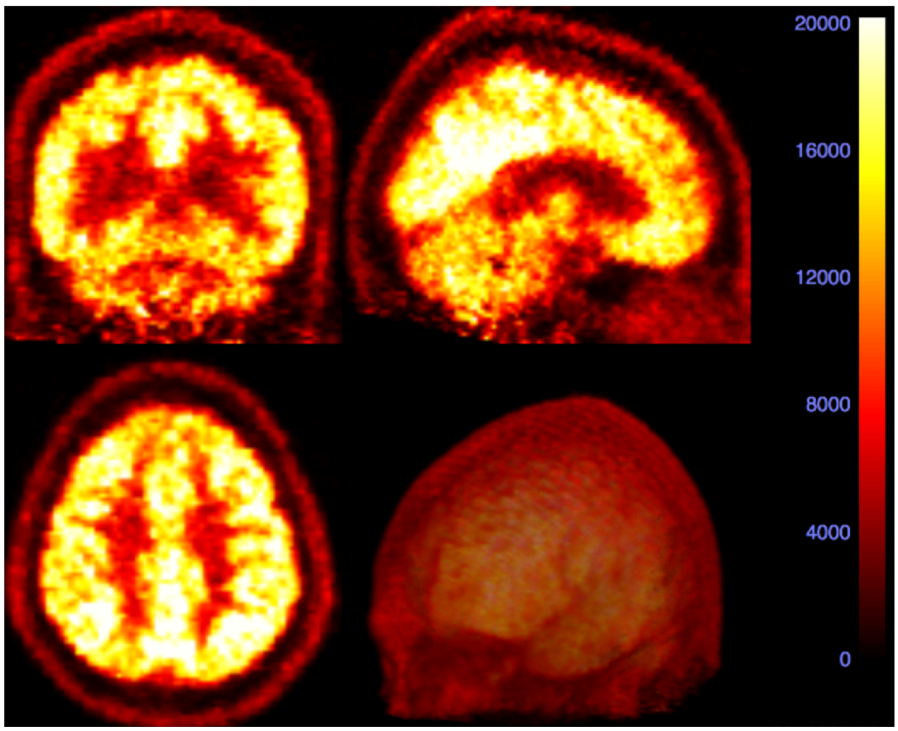

Figure 3.2: An example of PET static image in coronal (upper left), sagittal (upper right), axial (bottom left) and 3D projection (bottom right). The color scale used is "hot", to the right side, ranging from red to yellow.

3.2.2 A simple example

The model shown in Fig.3.3An example of compartment model.figure.caption.29 is a simple one-compartment model, with impulsive injection $u = D\delta(t)$ where δ is the Dirac operator, input rate P_1 and output rate K_{01}. The measure that can be obtained from this compartment is the concentration $C_1 = \frac{Q_1(t)}{V}$. The equation of this model is the following

$$\begin{cases} \dot{Q}_1 &= P_1 - K_{01}Q_1 + D\delta(t) \quad , \quad Q_1(0) = Q_{10} \\ C_1 &= \frac{Q_1(t)}{V} \end{cases}$$

3.2.3 General model

The general model for compartment model is the following:

$$\begin{cases} \dot{Q}_i &= \sum_{j \neq i} F_{ij}(Q_j) - \sum_{j \neq i} F_{ji}(Q_i) + P_i + u_i(t) \quad , \quad Q_i(0) = Q_{i0} \\ C_i &= \frac{Q_i(t)}{V_i} \quad \text{or} \quad C_i = 0 \end{cases}$$

In this case the i-th compartment gives at each moment the information Q_i to the

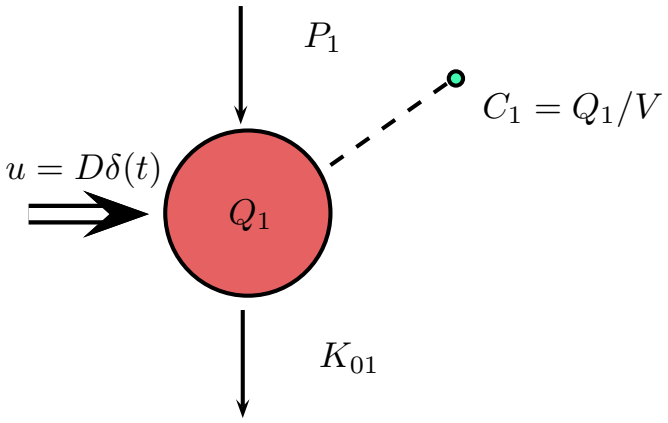

Figure 3.3: An example of compartment model.

j-th compartment at a speed $F_{ji}(Q_i)$, where the function F_{ji} can be eventually linear. It is possible to measure the concentration in some compartments. If this measure is missing, it is considered as zero.

3.2.4 Tracers

A **tracer** is a small quantity of substance used for the purpose of tracking a specific molecule called **traced**.
The tracer:

1. can be measured independently from the traced
2. follows the dynamics of the traced and do not perturb the state of the system (small quantity)
3. is kinetically indistinguishable from the traced

3.2.5 Indistinguishability principle

From the third assumption comes out the following principle:

$$P(\text{a particle leaving } j \text{ is tracer}) = P(\text{a particle in } j \text{ is tracer}).$$

This means that

$$\frac{f_{ij}}{F_{ij} + f_{ij}} = \frac{q_j}{Q_j + q_j}$$

or equivalently

$$\frac{F_{ij}}{Q_j} = \frac{f_{ij}}{q_j} = k_{ij}(Q).$$

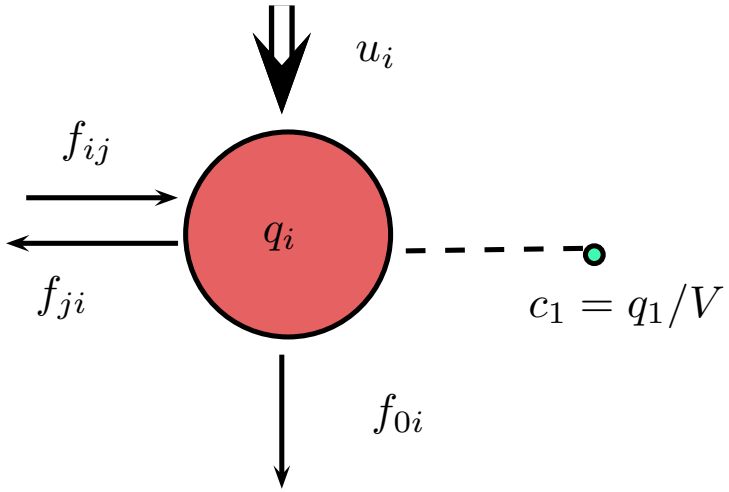

Figure 3.4: A general model for tracer kinetics. Only one of the n compartments is shown for shake of simplicity.

The general model for the kinetics of the tracer can be written as follows:

$$\begin{cases} \dot{q}_i &= \sum_{j\neq i} f_{ij}(Q,q) - \sum_{j\neq i} f_{ji}(Q,q) + u_i(t) \quad , \quad q_i(0) = q_{i0} \\ c_i &= \frac{q_i(t)}{V_i} \quad \text{or} \quad c_i = 0 \end{cases}$$

If all the functions $k_{ij}(Q) = k_{ij}$ are supposed constant then $f_{ij}(Q) = k_{ij}q_j$. In this case the model becomes linear:

$$\begin{cases} \dot{q}_i &= \sum_{j\neq i} k_{ij}q_j - \sum_{j\neq i} k_{ji}q_i + u_i(t) \quad , \quad q_i(0) = q_{i0} \\ c_i &= \frac{q_i(t)}{V_i} \quad \text{or} \quad c_i = 0 \end{cases}$$

3.2.6 A more general view

Under the hypothesis of linearity the model goes under the category of Linear Time-Invariant model and can be written in state-space form **LTI state-space** [2]

$$\begin{cases} \dot{x} &= Ax + Bu \quad , \quad x(0) = x_0 \\ y &= Cx \end{cases}$$

where u is the input, y the output and the system is determined by (A,B,C).

Theorem 3.2.1. *The system* (A, B, C) *is equivalent to the direct input-output relation*

$$y(t) = Cx(t) = (C\ \exp(tA)\ B) * u(t)$$

Proof Considering $\hat{x}$, the Fourier transform of x,

$$s\hat{x} = A\hat{x} + B\hat{u}$$

which is equivalent to

$$\hat{x} = (sI - A)^{-1}\ B\hat{u}.$$

and finally

$$\hat{y} = C\hat{x} = C\ (sI - A)^{-1}\ B$$

that leads to the thesis. □

By effect of Theorem 3.2.1theorem.3.2.1 the **impulse response function** (IRF) can be defined for such equations.

Definition 1. *Given the LTI system* (A, B, C)*, its IRF is the function*

$$\phi(t) = C\ \exp(tA)\ B$$

and its Fourier transform, the **Transfer Function**

$$\hat{\phi}(s) = C\ (sI - A)^{-1}\ B$$

so that $y = \phi * u$ *and* $\hat{y} = \hat{\phi}\hat{u}$.

Lemma 3.2.2. *Under the hypothesis the the input is a bolo,*

$$u(t) = D\delta(t)$$

, the Equation

$$y(t) = \phi(t) * u(t) =$$

becomes

$$y(t) = \phi(t) * D\delta(t) = D\phi(t).$$

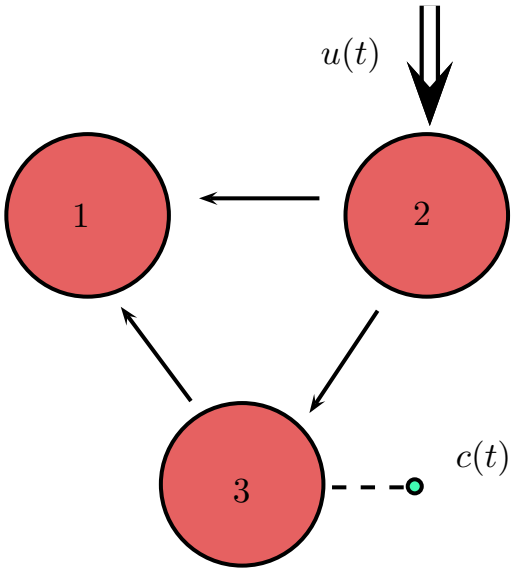

Figure 3.5: Is this model identifiable?

3.2.7 Identifiability and identification

Definition 2. *The model* (A,B,C)

$$\begin{cases} \dot{x} &= Ax+Bu \quad , \quad x(0)=x_0 \\ y &= Cx \end{cases}$$

is ***(uniquely) identifiable*** *if it is possible to determine (uniquely) the nonnegative entries of* A*, given* B,C*, and the* ***exact*** *data* x_0, y, u*.*

Observing the model in Fig.3.5Is this model identifiable?figure.caption.31, the reader wanders whether this model is identifiable or not. Next definitions and theorems will be helpful to solve many identifiability problems.

Definition 3. *1. A Compartment* k *is* ***in/out-put reachable*** *if* $\exists$ *a path from an in-out-put compartment to* k*.*

2. A system (A,B,C) *is* ***in/out-put reachable*** *if every compartment is in/out-put reachable.*

For instance, the system of Fig.3.5Is this model identifiable?figure.caption.31 is input reachable but not output reachable. Next theorems will link such property to identifiability.

3.2.8 Necessary and sufficient conditions

Theorem 3.2.3. (Necessary conditions): *Let* (A,B,C) *be an identifiable system, then:*

1. *The system is input reachable*

2. *Every compartment with an outgoing path is output reachable*

Again, taking the system of Fig.3.5Is this model identifiable?figure.caption.31, his reachability cannot be excluded or proved. Some other theorems are needed to achieve this goal.

Observation: The transfer function $\hat{\phi}(s)$ is a rational function of the form

$$\hat{\phi}(s) = \frac{N(s)}{D(s)} \text{ with } N \in \mathscr{P}^{n-1}, D \in \mathscr{P}^{n}$$

where $n = dim(A)$.

In fact

$$\hat{\phi}(s) = C\,(sI - A)^{-1}\,B = C\frac{adj(sI-A)}{det(sI-A)}B$$

and $adj(A) = \sum_{k=0}^{n-1} R_k s^k$

Theorem 3.2.4 (Sufficient conditions 1)**.** *In case the equations of the numerator and denominator have a (unique) solution, then the system* (A,B,C) *is (uniquely) identifiable.*

Theorem 3.2.5 (Sufficient conditions 2)**.** *If the equations* $\phi^{(k)}(0) = CA^kB, \quad for k = 0,\ldots,n-1$ *have a (unique) solution and the denominator is never null, then the system* (A,B,C) *is (uniquely) identifiable.*

The system of Fig.3.5Is this model identifiable?figure.caption.31 can be written as

$$A = \begin{pmatrix} 0 & k_1 & k_3 \\ 0 & -(k_1+k_2) & 0 \\ 0 & k_2 & 0 \end{pmatrix},$$

$$B = (0,1,0), C = (0,0,1/V_3)$$

and so by the theorems above it is finally possible to reach a conclusion: this model is identifiable, but not uniquely.

3.2.9 Identification

Identification can be made using the results of the two sufficient conditions, but such techniques have revealed to be numerically inaccurate. So the calculation of the parameters is given by a (weighted) nonlinear least squares method.

$$A = \arg\min ||y - y_A||^2 = ||y - \phi_A * u||^2 =$$
$$= ||y - (C \exp(tA)\, B) * u||^2$$

Of course nonlinear fitting using the original differential equations can be most of the times a reliable alternative.

3.2.10 Sokoloff Model

The Sokoloff model (1970s) is the main model studying the kinetics of the tracer ^{18}FdG in the brain. It uses a time sequence of PET images as measure and the injected tracer activity as input. Once fitted, the model provides the absolute glucose rate of that particular region of interest.

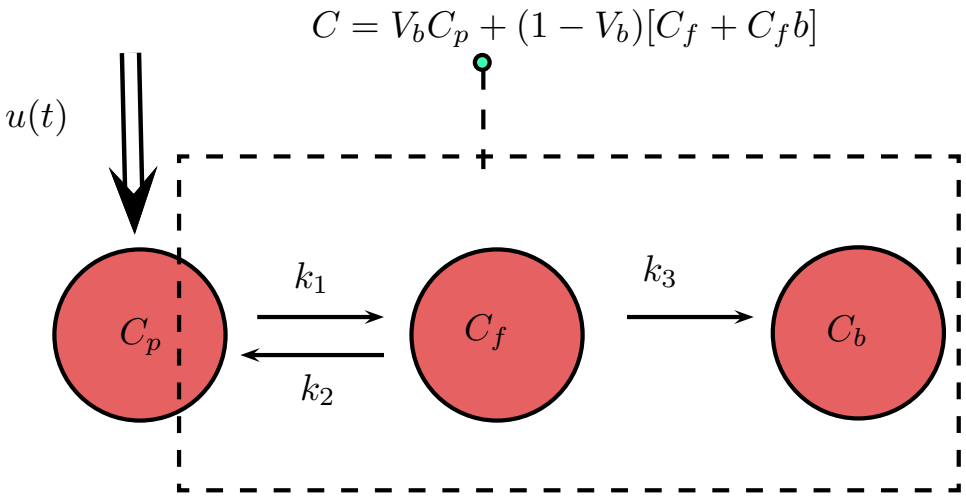

Figure 3.6: Sokoloff compartment model

This model is also known as 3K, as it is a three-compartment model with the hypothesis that the third compartment is irreversible. As the model has a unique data input, a (eventually PET-based) measure of the plasma glucose is needed for fitting this model. The model is the following, in LIT form

$$A = \begin{pmatrix} -k_1 & k_2 & 0 \\ k_1 & -(k_2 + k_3) & 0 \\ 0 & k_3 & 0 \end{pmatrix} \tag{3.2}$$

$$B = (1,0,0), C = (V_b, 1-V_b, 1-V_b).$$

By applying Theorem 3.2.5Sufficient conditions 2theorem.3.2.5

$$\det(sI - A) = s^3 + (k_1 + k_2 + k_3)s^2 - k_1 k_2$$

$$C\ adj(sI - A)\ B = V_b s^2 + (V_b k_1 + k_2)s.$$

and this proves that the Sokoloff model is identifiable, provided $C(t)$ and $C_p(t)$ are both known.

From the values k_1, k_2, k_3 it is possible to compute the value of the **local glucose metabolism** (or absolute Metabolic Rate of Glucose, aMRGlu)

$$MR = K\frac{\hat{C}_p}{LP}$$

where with this model

$$K = \frac{k_1 k_3}{k_2 + k_3},$$

$\hat{C}_p$ is concentration of glucose in the plasma (in stationary state) and LP is the lumped constant, used for correcting the difference between the plasma glucose and the measured PET value; it is usually set to 1 or 0.8.

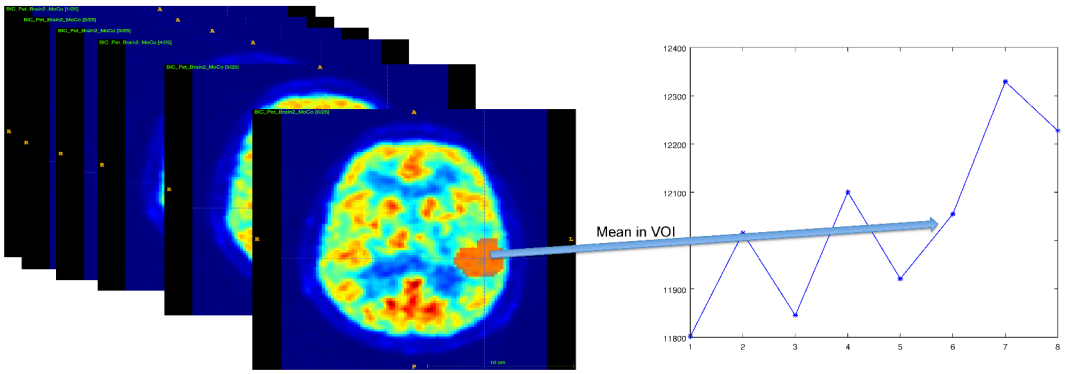

Figure 3.7: Graphical scheme for the computation of $C(t)$ from dynamical PET. For each image frame in the set, the mean value inside the Volume of Interest (VOI, in red overlay) is computed and collected to an array. This array represents the set of samples of $C(t)$.

3.2.11 Patlak fit method

Patlak fit method is a graphical method for the direct measure of aMRGlu [6]. As stated in the previous section, the measure of the Plasma Glucose $C_P(t)$ and the measured

Volume Of Interest (VOI) $C(t)$ are sufficient for the identification of the Sokoloff model. An easier and fastest way to identify the model is to use the relation

$$C(t) = K \int_0^t C_p(\tau)\, d\tau + V_b C_p(t) \tag{3.3}$$

Rewriting Equation 3.3Patlak fit methodequation.3.2.3 brings to light a linear dependence, in fact

$$\frac{C(t)}{C_p(t)} = K \frac{\int_0^t C_p(\tau)\, d\tau}{C_p(t)} + V_b \tag{3.4}$$

Hence, it is possible to compute K with linear fitting using least-squares methods.

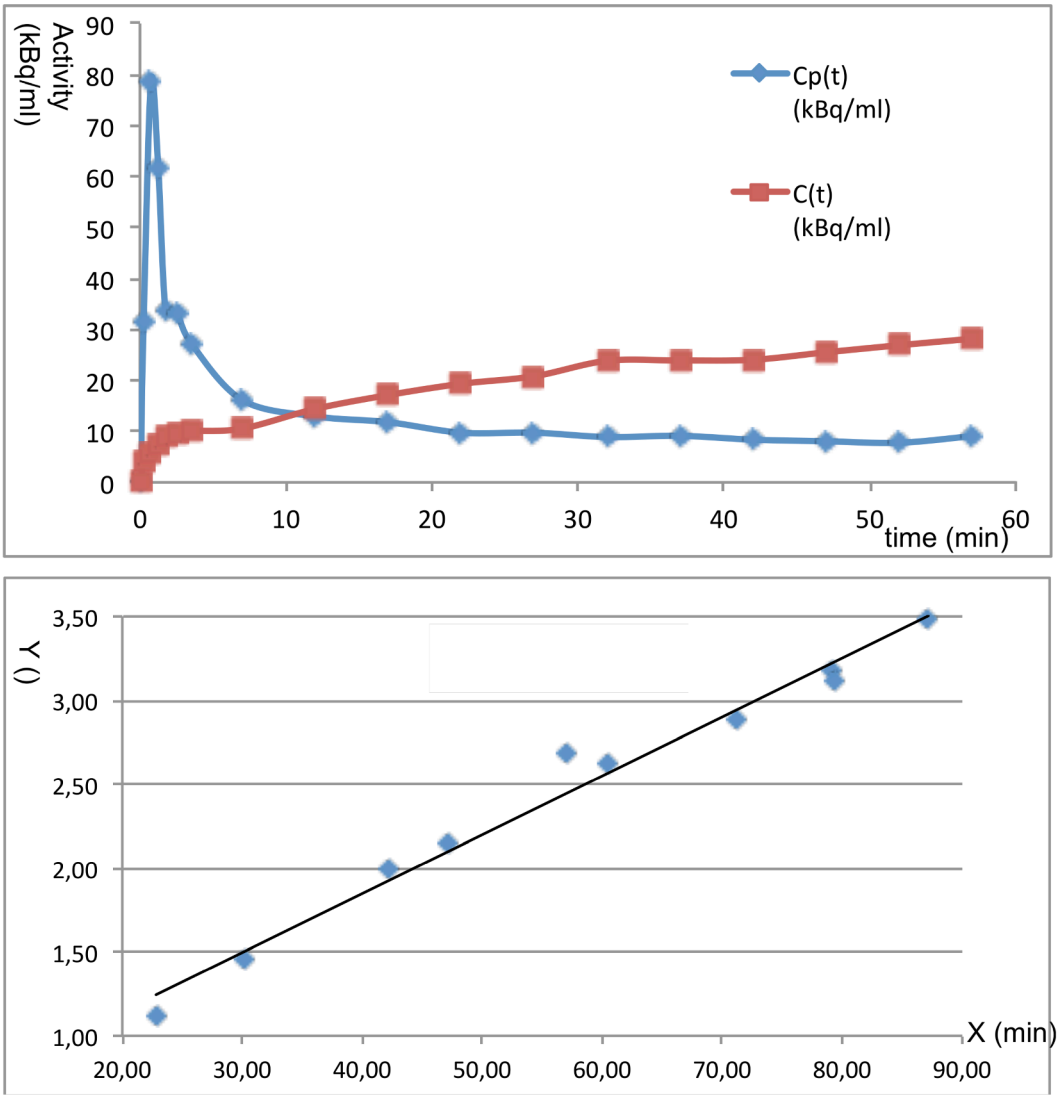

Figure 3.8: Example of Patlak fit. In the upper plot, the curves $C(t)$ and $C_p(t)$ over time. In the lower plot, the values of $X(t) = \frac{\int_0^t C_p(\tau)\,d\tau}{C_p(t)}$ versus the values of $Y(t) = \frac{C(t)}{C_p(t)}$ and the fitted line with slope K and intercept V_b. Note that, for a more stable fit, only the latter 10 samples are usually chosen.

Usually only the latter samples are chosen in order to improve the stability of the method, see Fig. 3.8Example of Patlak fit. In the upper plot, the curves $C(t)$ and $C_p(t)$ over time. In the lower plot, the values of $X(t) = \frac{\int_0^t C_p(\tau)\,d\tau}{C_p(t)}$ versus the values of $Y(t) = \frac{C(t)}{C_p(t)}$ and the fitted line with slope K and intercept V_b. Note that, for a more stable fit, only the latter 10 samples are usually chosen.figure.caption.34. This is made to avoid biases related to the uptake phase of the tracer, since it is wanted to express

the kinetics of the traced.
It is also possible to consider, instead of a number of VOIs, every voxel of the image. This approach is called voxel-wise, and will be treated in the next Chapter.

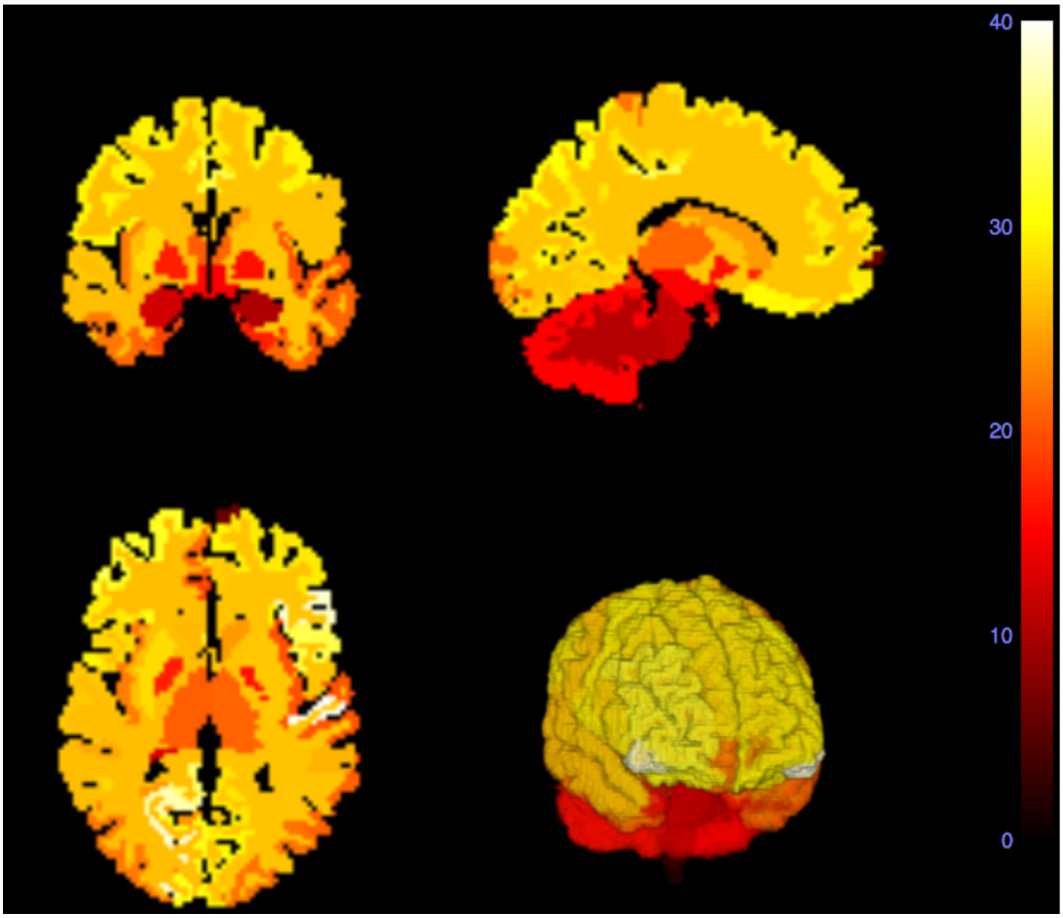

Figure 3.9: Image obtained by putting in each VOI of a segmentation map the corresponding value for aMRGlu in hot colormap, and 3D projection (bottom right).

Bibliography

[1] DH Anderson, *Compartmental Modeling and Tracer Kinetics*, Springer Berlin Heidelberg, 1983.

[2] RE Carson, P Herscovitch, ME Daube-Witherspoon, *Quantitative Functional Brain Imaging with Positron Emission Tomography*, Academic Press, 1998

[3] C Cobelli, E Carson, *Introduction to modeling in physiology and medicine*, AP, 2008

[4] C Cobelli, D Foster, G Toffolo, *Tracer kinetics in biomedical research*, Springer, 2001.

[5] ME Juweid, OS Hoekstra, *Positron Emission Tomography*, Humana Press, 2011.

[6] CS Patlak, RG Blasberg, *Graphical evaluation of blood-to-brain transfer constants from multiple-time uptake data. Generalizations*, Journal of Cerebral Blood Flow and Metabolism, 1985.

[7] D Poggiali, *Reconstruction of medical images from Radon data in transmission and emission tomography*, Master's thesis 2012.

[8] MN Wernick, JN Aarsvold, *Emission Tomography, The Fundamentals of PET and SPECT*, Elsevier, 2004.

Chapter 4

Most common algorithms for Neuroimaging

> S'accende il verde, innesto la marcia imballando il motore, sterzo tutto con la sinistra e nello stesso tempo alzo la destra al finestrino e sparo. L'uomo che inseguivo si piega sul volante. L'uomo che m'inseguiva abbassa la pistola ormai inutile. Io ho imboccato già la via trasversale. Non è cambiato assolutamente nulla: la colonna si muove con piccoli spostamenti discontinui, io sono sempre prigioniero del sistema generale delle macchine in marcia, in cui non si distinguono gli inseguitori e gli inseguiti.
>
> Italo Calvino, *Ti con Zero*

For computing the biomarkers from the images it is necessary to study, test and (whenever possible) improve many algorithms. From the accuracy of such algorithm it depends the order of bias and therefore the reliability of the results. Some of the useful and widespread algorithms used in MRI, PET and PET/MRI Neuroimaging pipelines will be treated in this chapter.
The chapter is organized as follows: in the First Section, some formal definitions will be given. The Second Section contains an introduction to Registration (or co-registration) algorithms, useful to align images one to another also from different sources. In the Third and Fourth Sections, Segmentation/Parcellation and Cortical Thickness evaluation algorithms will presented. Such algorithms are tuned mostly for MRI, but could be applied to PET if needed. Sections 5 and 6 contains methods used in PET and PET/MRI imaging. Section 7 contains a pipeline for PET/MRI studies that will be applied in the last Chapters.

All the most used programs for Neuroimaging have at least some Registration and Segmentation routines, many of them have also Cortical Thickness evaluation. It is less common to find a PET Kinetic Modeling, because it is a specific PET application.

4.1 A formal introduction

For a more precise description of the algorithm in use we shall introduce some mathematical definitions of the objects that will be used in the next Sections.

Definition 4. *An **image** can be considered as a function, say*

$$I : \Omega \subset \mathbb{R}^d \longrightarrow \mathbb{R}$$

with the dimension d usually set to 2,3 or 4, sampled over a grid of points

$$X = \{x_1, \dots x_p\} \;\; s.t. \;\; x_i \in \Omega$$

An image can be represented as a vector (with a slight abuse of notation)

$$\boldsymbol{I} = (I(x_i))_{i=1,\dots,n}$$

Note that the points in X can be eventually equispaced. If $d = 3$, X can be written in matrix 3D form

$$X_{i,j,k} = \left[x_{i,j,k}\right] \text{ s.t. } x_{i,j,k} \in \Omega \quad \forall\, i/j/k = 1, \dots N/J/K.$$

In that case the image is stored in form of a 3D $N \times J \times K$ matrix

$$\boldsymbol{I}_{i,j,k} = \left[I(x_{i,j,k})\right]$$

Definition 5. *A **segmentation** or **Volume Of Interest** (VOI) is an arbitrary subset of the domain $\Gamma \subseteq \Omega$ and its **mask** is a function*

$$\gamma(x) = \begin{cases} 1 & x \in \Gamma \\ 0 & x \notin \Gamma \end{cases}$$

It can be represented as a binary (3D/d-D) image, sampled at the same points X of a reference image I.

In Neuroimaging pratice, a VOI can tell where a given functional or morphological structure is. Of course, the human brain is made up by lots of VOIs, so another definition is needed. Given a VOI it is possible to measure some important features as the Volume of the VOI itself, given by the sum of the voxel times the voxel volume, or the mean[1] intensity of a co-sampled image.

[1] or standard deviation, or other statistical features.

Definition 6. *An **Atlas** (or deterministic Atlas) is obtained from a set of non-overlapping VOIs*

$$\Gamma_1, \ldots, \Gamma_n \quad s.t. \quad \Gamma_i \cap \Gamma_j = \emptyset \ \ \forall i \neq j$$

An atlas can be represented as a function

$$\mathscr{A}(x) = \begin{cases} i & \text{if } x \in \Gamma_i \\ 0 & \text{otherwise} \end{cases}$$

or equivalently (if $d = 3$) as a 3D image, sampled at the same points X of a reference 3D image I.
Another equivalent representation of an atlas is as a four-dimentional matrix $N \times J \times K \times n$, consisting in merged 3D binary representation of the VOIs.

In some situation the brain structures are detected from previous observation, thus given as a probability measure.

Definition 7. *A **Probability Map** is a set of functions mapping the domain Ω to the set $[0,1]$*

$$\mathscr{P} = \left\{ P_1, \ldots, P_n : \Omega \longrightarrow [0,1] \quad s.t. \quad \sum_{i=1}^{n} P_i \leq 1 \right\}$$

It can be represented (in $d = 3$ case) as a 4D image matrix $N \times J \times K \times n$, consisting in merged 3D image representation of the functions.

Note that an Atlas can be seen as a particular case of Probability Map. A Probabilistic Atlas can be transformed to a regular, deterministic Atlas by applying the maximum probability criterium

$$\mathscr{A}(x) = \arg \max_{i=1,\ldots,n} \tilde{P}_i(x) \tag{4.1}$$

with $\tilde{P}_i(x)$ defined as

$$\tilde{P}_i(x) = \begin{cases} P_i(x) & \text{if} \quad P_i(x) >= t \\ 0 & \text{if} \quad P_i(x) < t \end{cases}$$

for a given threshold $t \in [0,1]$ and for each $P_i \in \mathscr{P}$.

4.2 Registration

Registration of two medical images is a basic, fundamental algorithm in Neuroimaging. Suppose to have two images of the same subject acquired in two different sessions [4, 6, 7, 8]. The subject has possibly moved between sessions, so in order to catch the differences between the two scans an operation on the images is needed.

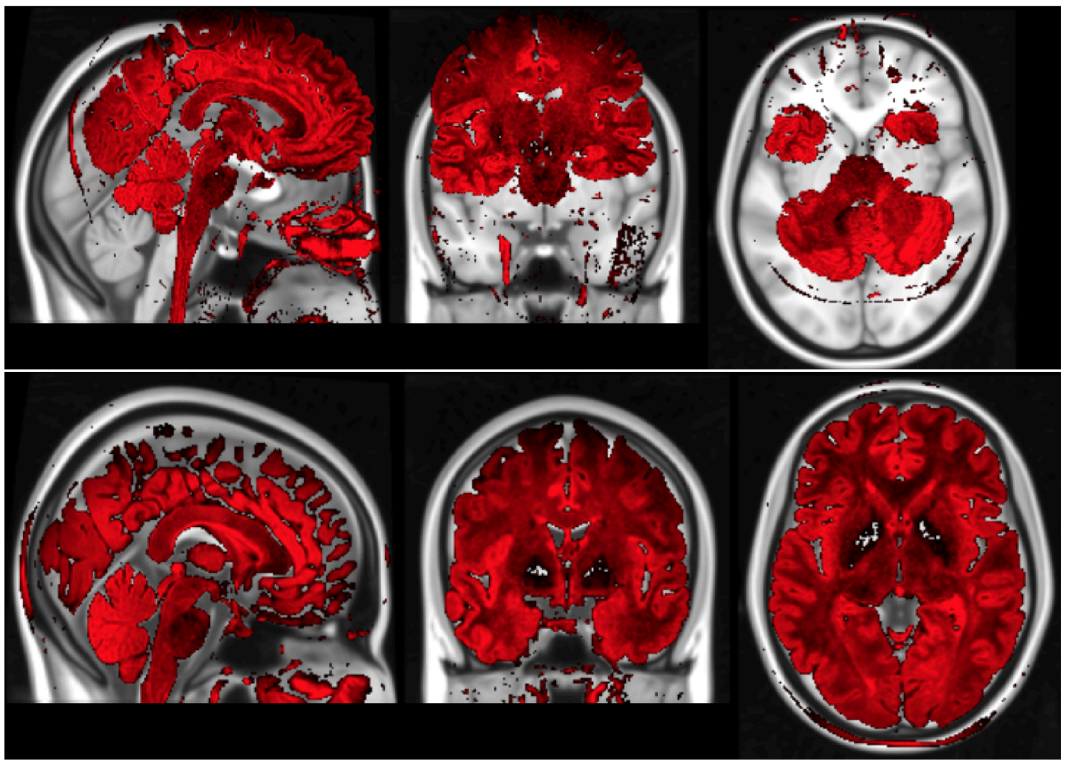

Figure 4.1: Reference image and target image (in red overlay) before (left) and after (right) rigid registration.

Definition 8. *Given a reference image R and an input image I, a* ***registration*** *is a function*

$$f : \mathbb{R}^3 \longrightarrow \mathbb{R}^3$$

such that $\mathscr{D}\left[R(x), I(f(x))\right]$ is minimal, given a distance (or pseudo-distance) $\mathscr{D}[.,.]$. The reference image R and the ***registered, output image*** *$I(f(x))$ is said to* ***lie in the same space****.*

The registering function f is found through an iterative scheme. The function can be of different forms.

Definition 9. *A function f in the form:*

- *$f(x) = b$ is a* ***translation****.*
- *$f(x) = Ax + b$ with $\det(A) = 1$ is a* ***rigid motion*** *or* ***rototranslation****.*
- *$f(x) = Ax + b$ with $\det(A) \neq 0$ is an* ***affinity****.*
- *$f(x)$ invertible is a* ***diffeomorphism****.*

A rigid registration is used when dealing with the same subject, assuming his head shape has not changed much between the two sessions. An affinity, or in some case a diffeomorphism, is used to put different subjects in the same space.

Also the distance can be different according to the needs. Some examples:

- **SSD**, sum squared differences

$$SSD[A,B] = 1/2 \int_\Omega (A(x) - B(x))^2 \, dx$$

- **NCC**, normalized cross-correlation

$$NCC[A,B] = 1 - \frac{\langle A,B\rangle^2}{||A||_2||B||_2}$$

  with the scalar product

$$\langle A,B\rangle = \int_\Omega A(x)B(x) \, dx$$

- **NGF**, normalized gradient-field

$$NGF[A,B] = \int_\Omega 1 - \langle g_\eta(A), g_\eta(B)\rangle^2 \, dx$$

  where the gradient-field is defined as

$$g_\eta(A(x)) = \frac{\bigtriangledown A(x)}{\sqrt{||\bigtriangledown A(x)||^2 + \eta}}$$

In practice NCC is used when registering the same subject with the same system (same MRI sequence, PET), since we can assume that the numerical values of the images did not change too much. In registering different MRI sequences NCC is a better option, while when registering two different modalities[2] NCC and NGF are equally reliable measures.

Since the registration process is an iterative algorithm, in some case registration programs can fail if the two images are too different in orientation. In Neuroimaging practice, this problem occurs in about 1/100 cases and it is solved by rotat ing and translating manually the input image to make it closer to reference.
A good trick for improving the speed of registration is to apply the registration algorithm to progressively undersampled versions of the image, obtained by averaging voxels squares[3] [6]. In this way the registration is progressively refined from a raw image (quicker to register) to the original one.

[2] e.g. registering a PET to a MRI image.

[3] e.g. $4 \times 4 \times 4$ voxels, $3 \times 3 \times 3$, $2 \times 2 \times 2$

4.3 Segmentation and Parcellation

Segmentation is the operation of dividing an image in VOIs on the base of morphological, intensity or functional features, eventually forming an atlas. For instance a very common segmentation of the human brain is using 2 classes, GM and WM or 4 classes: cortical GM (cGM), WM, deep GM (dGM) and CSF (mostly ventricles). **Parcellation**, in Neuroimaging contest, refers to a further subdivision of cGM into different classes according to the position and the surrounding sulci disposition.
Segmentation and Parcellation packages are included in all the popular Neuroimaging software suites as SPM, ANTs, FSL or freesurfer.

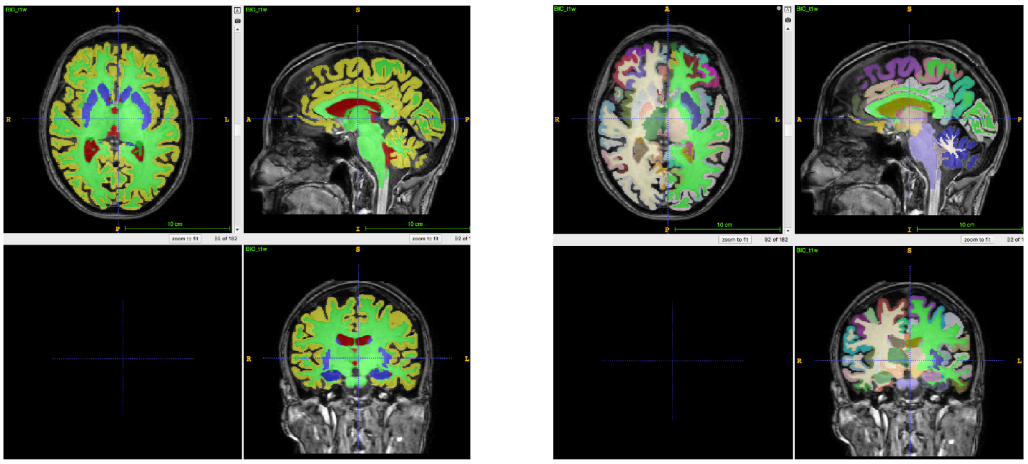

Figure 4.2: T1-weighted MRI image of a human brain with 4-class segmentation in overlap (left), parcellation of the cortex using freesurfer (right).

The basics of segmentation rely on registration algorithm. Suppose to have manually-segmented atlases from several brain images from different subjects. Registering all the images to the same space and average all the 4D atlases registered to common space with the same function gives birth to a probabilistic map. The probabilistic map is a good first guess for automatical segmentation of another, unsegmented brain image registered to the same space as above.
At this point a number of methods for refining the probabilistic map to a reliable segmentation have been proposed, from simple maximum probability

$$\mathscr{A}(x) = \arg\max_i \mathscr{P}_i(x)$$

to more sophisticated methods as label fusion majority vote, used by ANTs [10] or geodesic flow [1].

4.3.1 How to quantify the goodness of a segmentation

Manually segmented atlases are commonly considered as the gold standard. So, in order to quantify the error between a manually segmented VOI and one obtained automatically some measures have been defined.

Definition 10. *Given two VOIs A and B, expressed in form of set containing the 1-valued voxels, it is possible to define:*
the dice coefficient *or Soreson Coefficient*

$$Q_s = \frac{2|A \cap B|}{|A| + |B|}$$

the Jaccard index

$$J = \frac{|A \cap B|}{|A \cup B|}$$

with $|\cdot|$ the cardinality of the set, equivalent to the sum of the values of the VOI in matrix form.

Both indexes take values in $[0,1]$. Interestingly, the relation between the two can be proved to be $Q_s \geq J$ and $Q_s = J$ if and only if both are 0 or 1. This means that in practice Jaccard index is more severe about small differences between VOIs.

4.3.2 Pre-segmentation Correction Methods

Before applying segmentation algorithm it is a good practice to apply some correction algorithms, in order to reduce segmentation errors.
First of all in brain MRI, it is necessary to correct the bias due to inhomogeneity of the field B_0, which in practice is not completely stationary. Most used algorithms are called N3 and N4[9] Bias Field Correction. Another approach suggests to measure the field with the MRI directly.
Another common useful operation is to find a brain tissue mask in order to isolate the brain tissue from the surrounding meninges, dura mater, bones, eyes and other tissue. This operation is referred as skull-stripping.
In some neurological illness as MS, T1-hypointense lesions appear in the brain, affecting the segmentation quality. The correction most in use is called lesion filling[2]. This approach proposes to inpaint WM lesion putting inside the lesion mask intensity values more similar to the surrounding Normal Appearing WM (NAWM). It has been proven that the segmentation obtained after fiilibg has improved dice and Jaccard coefficient when comparing to manual segmentation.

4.4 Cortical Thickness

Cortical Thickness (CTh) is a widespread biomarker in Neuroscience. It decreases with natural aging, and has been proved to decrease faster in presence of several Neurological illnesses, including MS and AD. There is not currently a formal definition corresponding to the intuitive idea of mean thickness of the cortex, and no gold standard has been found at the moment.

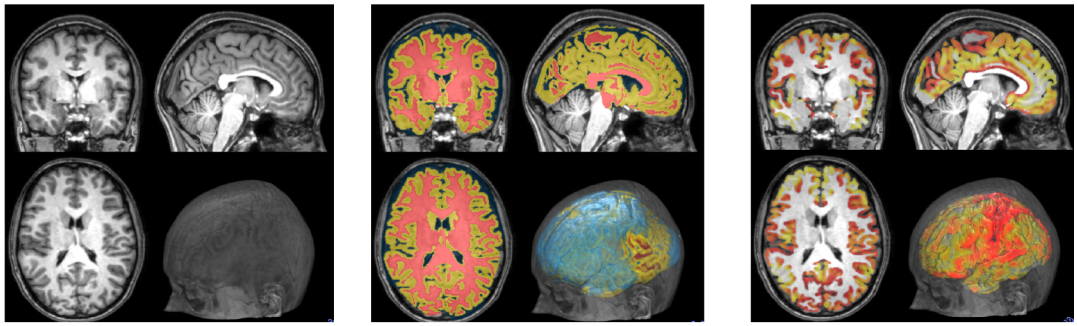

Figure 4.3: T1-weighted MRI image of a human brain (left), WM-GM segmentation in overlap (center), Cortical thickness image in jet map overlap (right).

4.4.1 A method for Cortical Thickness evaluation

Between all the methods for CTh computation, the author has chosen to show Diffeomorphic REgistration based Cortical Thickness (DiRECT) [3] due to its mathematically elegant formulation.
GIven a brain image

$$P(x) : \Omega \subseteq \mathbb{R}^3 \longrightarrow \mathbb{R}$$

segmented in three binary masks

$$P_g + P_w + P_c = 1$$

representing GM, WM, CSF respectively, the gray-white matter interface is defined as

$$GWI = P_g \cup dil_1(P_w)$$

and the brain tissue mask as

$$P_{wg} = P_w \cup P_g.$$

In a similar way to Level-set methods, the algortithm will look for the diffeomorphism

$$\phi : \Omega \times [0,1] \longrightarrow \Omega$$

such that:

- $\phi(x,0) = x$
- the thickness is contrained, $\left|\phi(x,1) - \phi(x,0)\right| < \tau$ for each $x \in GWI$
- there exists a velocity field $\Omega \times [0,1] \longrightarrow \mathbb{R}^3$ such that

$$\frac{d\phi}{dt} = v(\phi(x,t),t)$$

or equivalently

$$\phi(x,t) = x + \int_0^t v(\phi(x,t),t)\, dt$$

This function ϕ is meant to be a continuous map between the GWI and the exterior of the cortex. The idea of this approach is not to explicitly give the exterior of the cortex in order to compute a correct value even in presence of segmentation error between the cortex and the dura. On this purpose it is necessary to give a condition $\left|\phi(x,1) - \phi(x,0)\right| < \tau$ where τ usually set to 4 or 5 is the maximum value of the cortical thickness.

Equivalently, the diffeomorphism ϕ minimizes the functional

$$E(\phi(x,1)) = \int_0^1 ||v(x,t)||^2\, dt \;+\; \left|\left|P_w(\phi(x,1)) - P_{wg}(x)\right|\right|^2$$

subject to:

$$\phi(x,t) = x + \int_0^t v(\phi(x,t),t)\, dt$$

$$T(x) = \left|\phi(x,1) - \phi(x,0)\right| < \tau \;\; \forall x \in GWI$$

At this point the optimal solution ϕ is computed with an iterative scheme, and the function $T(x)$ is the measure of the thickness of the cortex, as wanted.

4.5 Motion Correction and Partial Volume Correction

This Section concerns some algorithms used in PET for correcting some issues linked to the nature of the PET system.
First of all motion. List-mode PET[4] can last up to 30 minutes, and the patient happens to move a little in this time. In order to reduce this source of bias, Motion Correction is applied.

[4] or PET time series, resulting in a 4D image, made up by 3D PET images called frames.

Motion correction is a simple operation: the average 3D image is computed by averaging all the voxels in time dimension. Once obtained, the average image[5] is treated as reference for rigid registration of each of the 3D images of the single PET frames. The registered frames are merged to a new 4D PET image. As can been observed in Fig. 4.4PET averaged image of a MS subject before (up), and after (bottom) motion correction.figure.caption.40, Motion correction improves the definition of the averaged PET image.

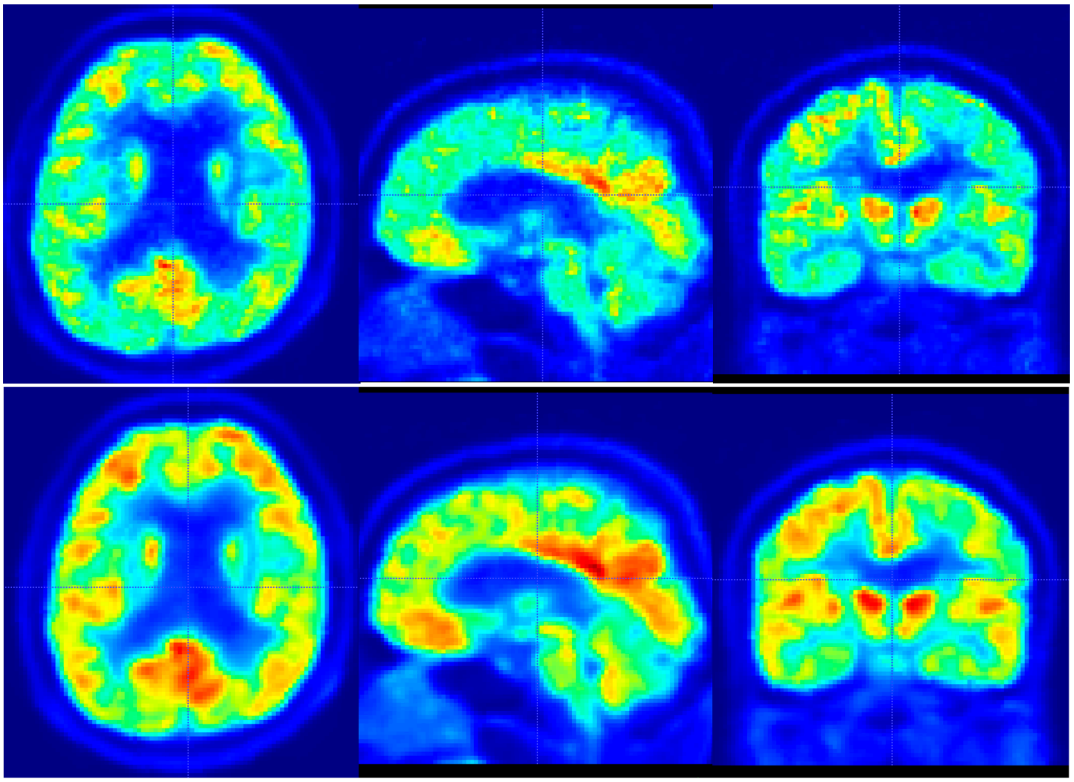

Figure 4.4: PET averaged image of a MS subject before (up), and after (bottom) motion correction.

[5] eventually registered to a MRI or CT anatomical image from which is possible to obtain a good segmentation atlas.

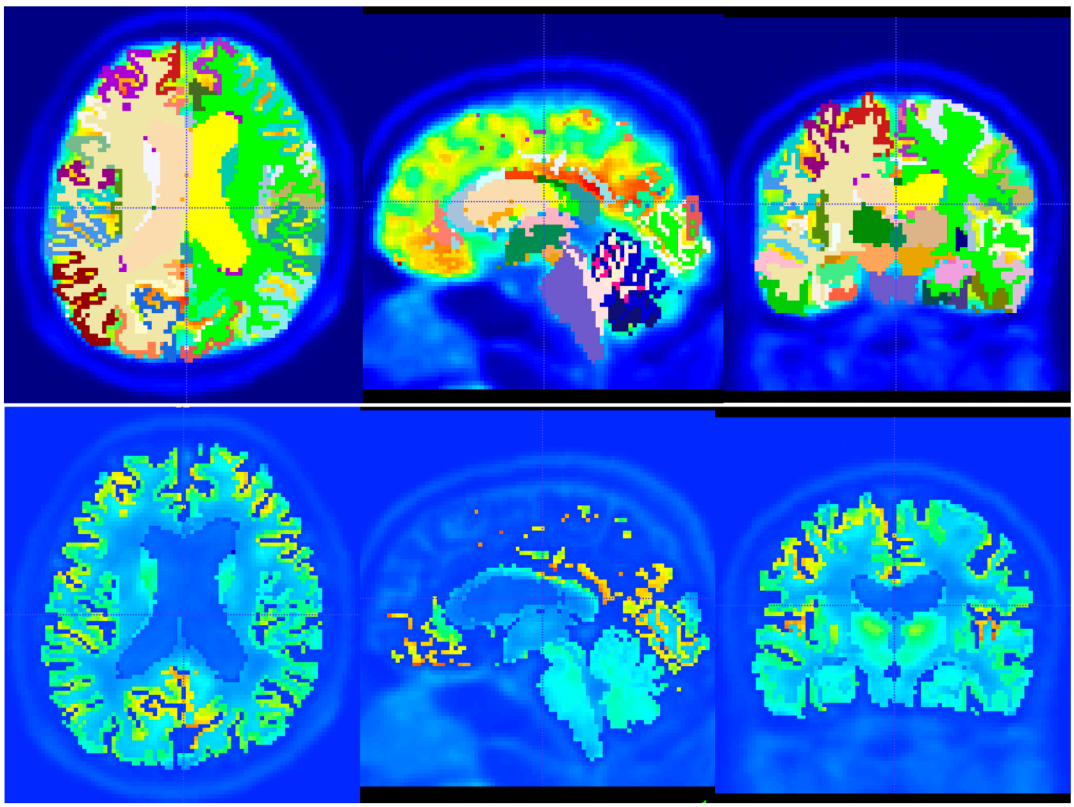

Figure 4.5: After motion correction the atlas (up, in overlay) is used for PVC. The result (bottom) is an image with greater spatial resolution.

After motion correction it is nowadays considered as mandatory to correct the Partial Volume Effect. PET system has a lower resolution compared to MRI, its FWHM can range from 4 up to 6 mm. In order to attempt to compute a more precise measure, one can try some raw methods as a simple deconvolution using a Point Spread Function obtained by scanning a Point-wise source as a little sphere with some tracer on. A good alternative is to use the atlas obtained by segmenting a coregistered anatomical image. This approach is called VOI-based Partial Effect Correction (PVC), and many algorithms are written using this approach [5]. In Fig. 4.5After motion correction the atlas (up, in overlay) is used for PVC. The result (bottom) is an image with greater spatial resolution.figure.caption.41 it is possible to observe that after a VOI-based PVC the PET image has improved much in resolution.

4.6 Kinetic Models estimation

There are two ways to obtain biomarkers from PET data: SUV/SUVR or kinetic modeling. The first one is the Standardized Uptake Value (SUV) of a VOI from a 3D static

PET or from a mean image of 4D list-mode PET. SUV is defined as

$$SUV(VOI) = \frac{SUV(VOI)}{C_{inj}}$$

the mean value in the VOI divided by the injected tracer activity. In case the injected activity is unknown, it is possible to compute the SUV Ratio (SUVR) as

$$SUVR(VOI) = \frac{SUV(VOI)}{SUV(Ref)} = \frac{mean(PET(VOI))}{mean(PET(Ref))}$$

with Ref a reference VOI, usually the whole brain VOI, or an area that is proved not to be involved by the illness[6].

The second way is to validate a kinetic model for the specific PET tracer in use[7]. Once a model is validated, fitting the model data (as explained in Chapter 3) outcomes the parameters value. From such parameters it ipossible to compute many biomarkers.
Of course it would be better to give a *physical* meaning to the biomarkers in order to give the clinician results to be read and interpreted correctly.

4.7 A faster computation for pixelwise Patlak

As stated in previous Chapter, the commonly adopted model in the case of tracer ^{18}Fdg is Sokoloff model and a simple way to obtain the absolute glucose rate aMRGlu is the Patlak linear fit.

As seen in Chapter 3, the absolute metabolic rate aMRGlu is proportional to the coefficient K, which can be recovered by fitting

$$\frac{C(t)}{C_p(t)} = K\frac{\int_0^t C_p(\tau)\,d\tau}{C_p(t)} + V_b \tag{4.2}$$

[6] In most cases, it can be the cerebellum cortex/WM or in some case the WM.
[7] this requires several subject scans as training data.

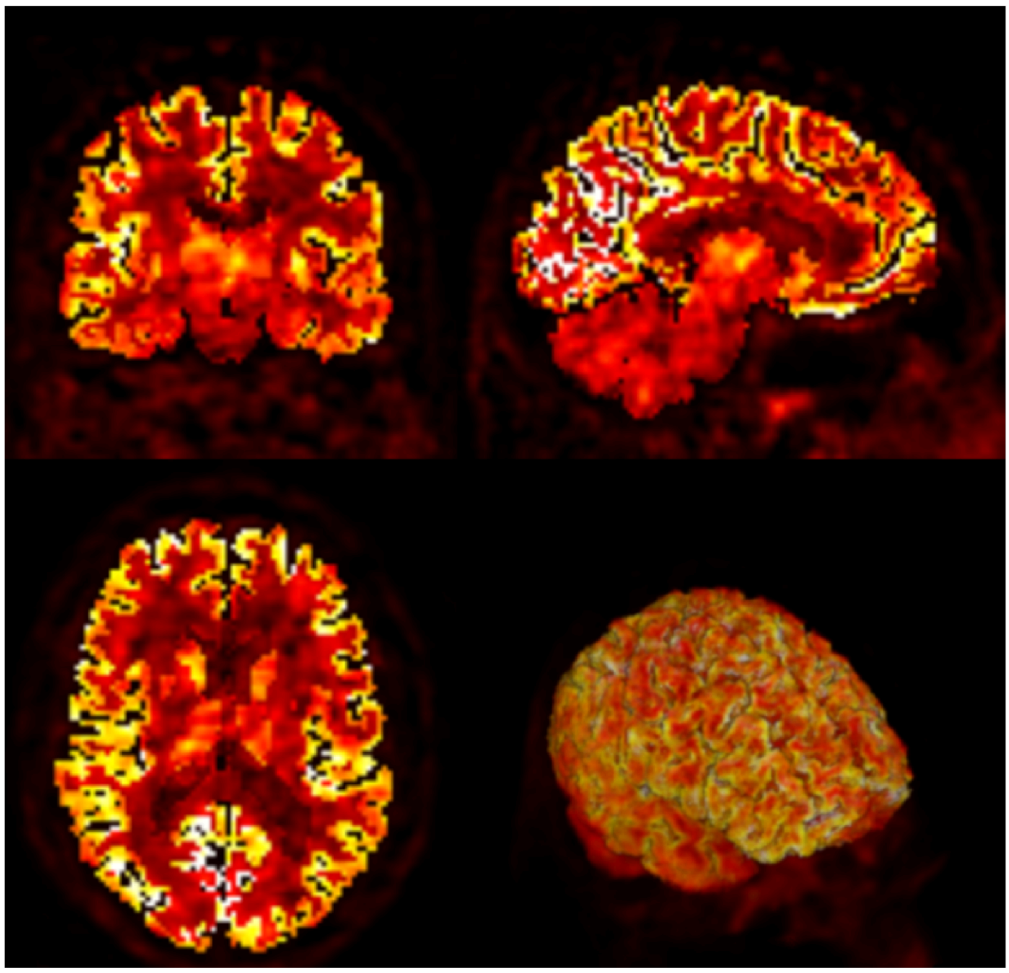

Figure 4.6: Pixelwise parametric image for Sokoloff model.

It is possible to rewrite Eq. 4.2A faster computation for pixelwise Patlakequation.4.7.2 as

$$(\boldsymbol{X}, 1) \cdot \begin{pmatrix} K \\ V_b \end{pmatrix} = \boldsymbol{Y} \tag{4.3}$$

with $\boldsymbol{X}$ and $\boldsymbol{Y}$ the vectors of length n in which are stored respectively the values of $\frac{\int_0^t C_p(\tau)\,d\tau}{C_p(t)}$ and $\frac{C(t)}{C_p(t)}$ for $t = t_1, \ldots, t_n$, and $\mathbf{1}$ is the unit vector of length n. Now normal equations for this system are

$$\begin{pmatrix} \boldsymbol{X} \cdot \boldsymbol{X}^T & sum(\boldsymbol{X}) \\ sum(\boldsymbol{X}) & n \end{pmatrix} \begin{pmatrix} K \\ V_b \end{pmatrix} = \begin{pmatrix} \boldsymbol{X} \cdot \boldsymbol{Y}^t \\ sum(\boldsymbol{Y}) \end{pmatrix} \tag{4.4}$$

where the function $sum(\boldsymbol{X}) = \boldsymbol{X} \cdot \mathbf{1}$ is simply the scalar sum of all the array values and $\boldsymbol{X}^T$ is the transpose of $\boldsymbol{X}$. Eq. 4.4A faster computation for pixelwise Patlakequation.4.7.4

can be solved with ease; the solution is

$$K = \frac{n\boldsymbol{X}\cdot\boldsymbol{Y}^T - sum(\boldsymbol{X})sum(\boldsymbol{Y})}{n\boldsymbol{X}\cdot\boldsymbol{X}^T - sum(\boldsymbol{X})sum(\boldsymbol{X})}$$

$$V_b = \frac{sum(\boldsymbol{X})}{n} - K\frac{sum(\boldsymbol{Y})}{n}.$$

It is also possible to compute the standard deviation for the slope K

$$SD = \sqrt{\frac{1}{n-2}\frac{\left(\boldsymbol{Y}-\tilde{\boldsymbol{Y}}\right)\cdot\left(\boldsymbol{Y}-\tilde{\boldsymbol{Y}}\right)^T}{\left(\boldsymbol{X}-\frac{sum(\boldsymbol{X})}{n}\right)\cdot\left(\boldsymbol{X}-\frac{sum(\boldsymbol{X})}{n}\right)^T}}$$

where $\tilde{\boldsymbol{Y}}$ is the vector of estimated values

$$\tilde{\boldsymbol{Y}} = K\boldsymbol{X} + V_b.$$

In case the pixel-wise image is going to be computated, it is computationally inefficient to compute the value of K for each voxel singularly. The number of voxels in a 3d image can be of the order of 10^6. A faster way can be to store all the values of the vectors $\boldsymbol{X}$ in a matrix, which will be called with a slight abuse of notation $\boldsymbol{X}$, and compute the vector K using the same solution as before. Parallel calculus for matrix multiplication, already implemented in several programming languages, will speed up the computing time.

4.8 Pipelining

A pipeline is a sequence of operation to be applied to every subject's images in order to obtain the desired biomarkers. In this section a sample study shall be presented.
Suppose to have a dataset of at least 30 MS patient, all undergoing MRI with sequences: T1, FLAIR and DIR. The goal of the study is to obtain volume values for WM and GM lesions for each VOI in a morphological atlas, obtained by segmenting T1 using manual segmentation or, more easily, a fully automated software as freesurfer.
Even if this task seems easy, many operations are needed in order to obtain the requested measures with minimal bias. First of all, T1 has to be corrected for Bias-Field and Lesion-Filling, before segmentation. Furthermore, all lesion masks and anatomical atlas have to lie in the same space. For simplicity, an usual choice could be to move FLAIR and DIR in T1 space before manual segmentation.
Once we have the atlas from T1 and the WM lesion and GM lesion masks, it is easy to compute the volume of WML and GML in each VOI of the atlas by

$$Vol(Mask, VOI) = dV\ |Mask \cap VOI|$$

where $|\cdot|$ is the number of the voxel in the intersection and dV is the Volume (say in mm^3) of a single voxel, which can be easily found in the image metadata.
Fig 4.7The flowchart of this sample MS pipeline. Squares represent the images, Circles the operations, Trapezoids masks and atlases, Double squares with rounded corner the numerical results.figure.caption.43 contains a graphical representation of the sample pipeline presented above.

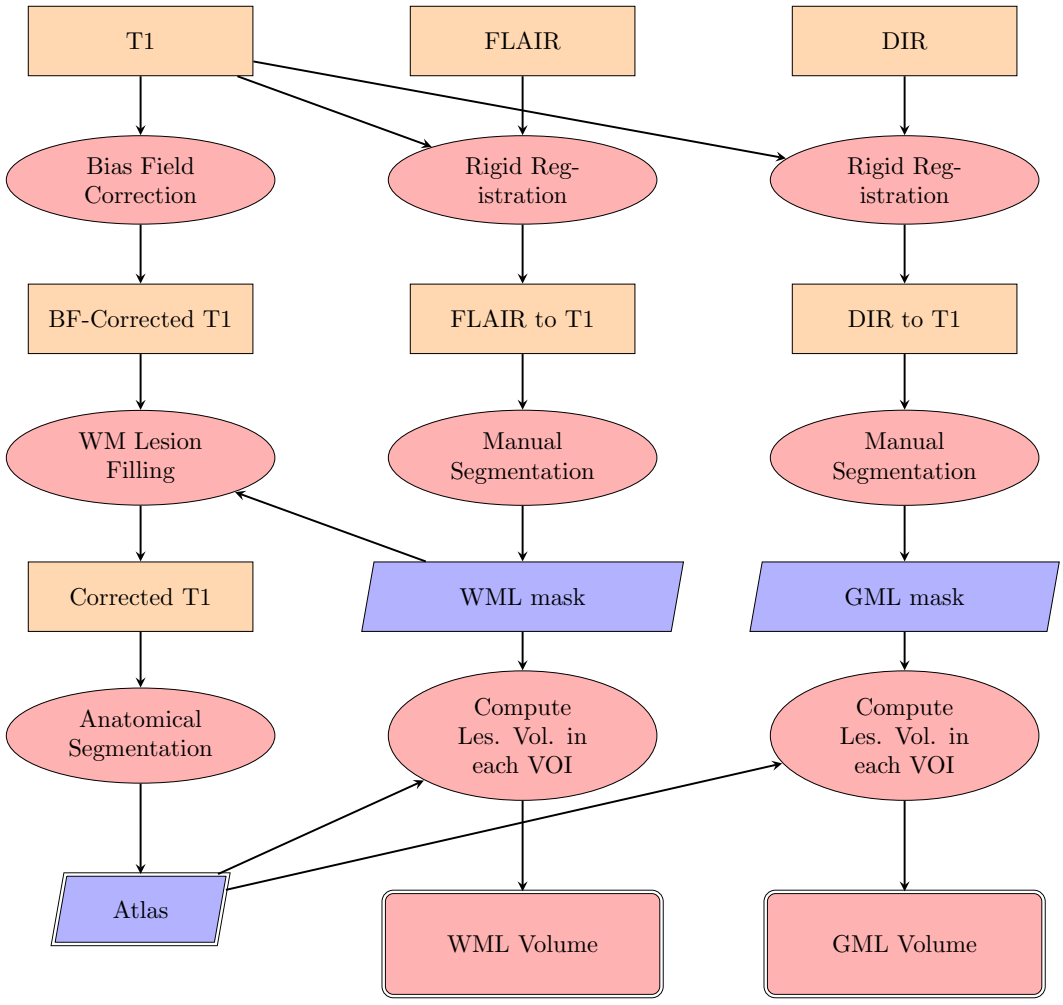

Figure 4.7: The flowchart of this sample MS pipeline. Squares represent the images, Circles the operations, Trapezoids masks and atlases, Double squares with rounded corner the numerical results.

Bibliography

[1] MJ Cardoso, R Wolz, et al., *Geodesic information flows*, Med Image Comput Comput Assist Interv. 2012

[2] DT Chard, JS Jackson, DH Miller, CA Wheeler-Kingshott, *Reducing the impact of white matter lesions on automated measures of brain gray and white matter volumes*. J Magn Reson Imaging. 2010

[3] SR Das, BB Avants, M Grossman, JC Gee, *Registration based cortical thickness measurement*, Neuroimage. 2009

[4] G Dougherty, *Digital Image Processing for Medical Applications*, Cambridge University Press. 2009

[5] K Erlandsson, I Buvat, PH Pretorius, BA Thomas, and BF Hutton, *A review of partial volume correction techniques for emission tomography and their applications in neurology, cardiology and oncology*, Phys. Med. Biol., 2012.

[6] JV Hajnal, D Hill and DJ Hawkes, *Medical Image Registration*, CRC Press. 2001

[7] J Modersitzki, *Numerical Methods for Image Registration*, Oxford University Press. 2004

[8] J Modersitzki, *FAIR: Flexible Algorithms for Image Registration*, SIAM. 2009

[9] Tustison NJ, Avants BB, Cook PA, et al. *N4ITK: Improved N3 Bias Correction*, IEEE transactions on medical imaging, 2010.

[10] H Wang, SR Das, et al., *A learning-based wrapper method to correct systematic errors in automatic image segmentation: consistently improved performance in hippocampus, cortex and brain segmentation* Neuroimage. 2011

Chapter 5

A MS study in PET/MRI

> "Incominciamo male!" ho pensato davanti al medico legale della Asl di via Luzzatti. Ero davanti a lui perché doveva autorizzare il rilascio per il mio permesso invalidi. Questo signore, molto presumibilmente laureato, dopo avermi visitato e aver visionato i 750 certificati che sanzionavano inesorabilmente la mia sclerosi multipla galoppante, con fare professionale ha decretato: "Lo autorizzo per due anni, poi vedremo come procede".
>
> Fiamma Satta, *Diario*

The ongoing of Multiple Sclerosis in MRI and other imaging techniques have been studied under several points of view, but (at present date) no published research included brain metabolism yet. PET glucose tracer ^{18}Fdg allows the computation of the absolute Metabolic Glucose Rate (aMRGlu), which is a good biomarker indicating the brain activity. In this chapter a pilot study with PET/MRI involving 31 patients is presented.

5.1 Introduction

The relationship between inflammatory processes and atrophy in MS is still unraveled, and studying the metabolism could offer an important, missing ring of this chain.
Microglial activation in the early phases of MS may lead to several metabolic effects on synapses and neurons, causing a progressive neuronal loss and GM atrophy, inducing metabolic changes in the cortex in a first phase and then determining synapsis and neuronal loss and atrophy.
Under this hypothesis, it could be possible to prove the presence of changes in cortical

metabolism before atrophy. Longitudinal studies [5, 4] lead on AD seem to confirm this idea.

5.2 Materials and Methods

5.2.1 Patients

Two groups of MS patients were enrolled in the study:

- 14 CIS suggestive of MS (7 patients) or early RRMS (eRRMS, 7 patients) with short disease duration (DD 1.7±0.33) and no sign of cognitive impairment.
- 15 RRMS with a longer DD (19.1±10.0) and clear signs of cognitive impairment.

In order to avoid age-related biases, the age of the two groups was selected in the range between 22 and 57 years. No significant difference of age was found between these two groups. The study was approved by the local Ethics Committee that, however, did not give the permission of enrolling normal controls in the study. All patients gave written informed consent.

5.2.2 MRI and PET

The following MRI images of every patient were acquired on a PET/MRI 3T Siemens System (BiographmMR PET Siemens)

- T2 coronal thoracic short tau inversion recovery space (STIR) for Aorta segmentation.
- 3D T1 MPRAGE of the brain for brain segmentation and parcellation.
- 3D brain FLAIR for WML detection.
- 3D brain DIR for GML detection.

To the PET side, an injection of ^{18}Fdg glucose tracer was injected in each patient. After the injection the PET was acquired in thorax and brain in three different sessions: early thorax (TOR1), late thorax (TOR2) and late brain (BRAIN2).
This subdivision was made in order to accurately estimate the plasma glucose from the aorta VOI in TOR1 and TOR2 images and to let the patient rest a while between the early and late acquisition.

The choice of recovering the input function $C(t)$ from the aortic tract is slightly different from the usually-adopted strategies: usually the input function is derived

either by arterial sampling, which is the golden standard but it is also very invasive, or by carotid/brain vessels PET images. This last option is the most used, since the carotid/brain vessel signal comes *for free* with the brain PET. However, such signal might be very poor because of the Partial Volume Effect. This is not such a big problem for aortic tract, since there is no surrounding body with such high tracer signal.
Even if the aorta-approach has proven in our environment to be consistent with arterial sampling, it has not been proven yet to obtain better results than the carotid-approach.

5.2.3 Pipeline

The purpose of this study is to obtain absolute Metabolic Rate of Glucose (aMRGlu) and Cortical Thickness (CTh) values for the cortical parcels of DTK atlas, extracted with freesurfer. To approximate the plasma glucose $C_p(t)$ it has been chosen to obtain PET/MRI images of the thorax right after the injection (TOR 1) and after 30 min (TOR 2), in order to recover C_p from the Aortic VOI. After TOR2, the scanner moves to the head to acquire (Brain).
Now, assuming that each PET is aligned to the relative MRI, the best way for registering PET TOR1 to PET TOR2 is to align the two relative MRIs and apply the transformation to PET. Once the Aorta VOI is manually segmented, it is easy to get an aortic Time Activity Curve (TAC) by averaging the two PET inside the Aorta VOI.
For what concerns the anatomy, MRI is rigidly registered to a template so that the bicommissural line is horizontal in Sagittal view and the real size of a voxel is $1mm$ per size. This orientation will be referred as BIC space. PET Brain is also aligned to BIC using the same transformation as its MRI, then motion correction and PVC are applied.
The T1 MRI sequence is processed using Freesurfer and the resulting atlas is registered to the BIC space. Freesurfer also provides an estimation of CTh for all the cortical parcels of the atlas. After having obtained the TAC $C(t)$ for each VOI of the atlas by averaging, it is necessary to interpolate $C_p(t)$ to the same timepoints of the brain.
At last, Patlak fit method is applied to obtain aMRGlu value for each VOI of the atlas. In Fig 5.1The sample flowchart of the PET/MRI pipeline discussed.figure.caption.45 it is possible to see a flowchart representation of the pipeline. Patlak fit method was also applied voxel-wise resulting in aMRGlu parametric images.

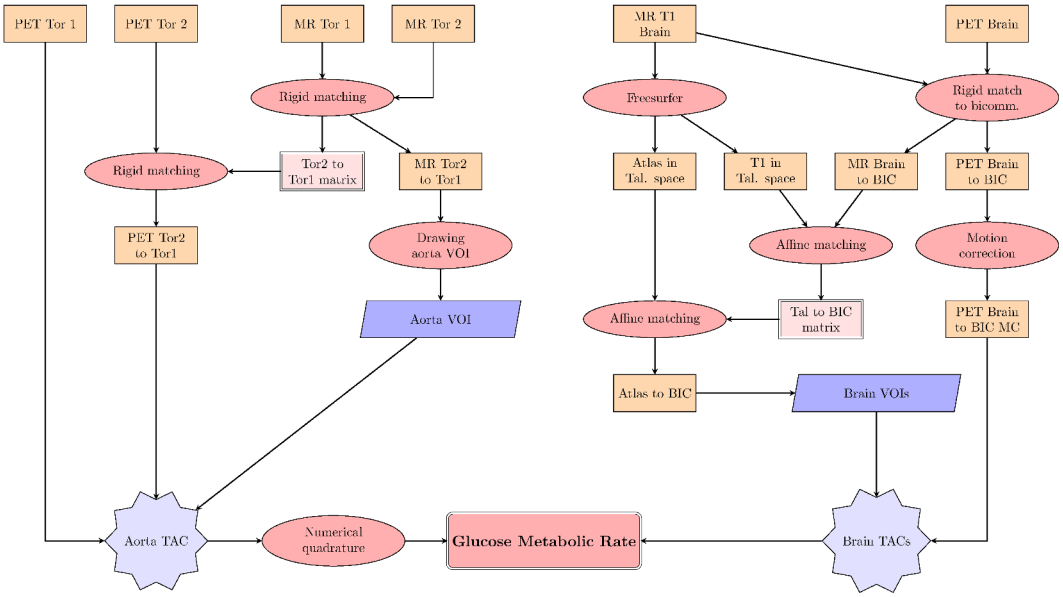

Figure 5.1: The sample flowchart of the PET/MRI pipeline discussed.

Figure 5.2: Coronal view of thoracic MRI and manually drawn aorta VOI (in red overlay).

Moreover, WML and GML masks were manually extracted from MRI FLAIR and DIR sequences in order to obtain the number and volume of lesions of each VOI in the Freesurfer-obtained atlas. Results were also averaged by lobes: Frontal, Temporal, Occipital, Parietal, Insular for cortical Areas and Central, Posterior Fossa for Subcortical

areas.

5.2.4 Statistics

When comparing two groups, their normality was checked using Shapiro-Wilk test and homoscedasticity using F-test. Then, the two groups were compared using unpaired t-test and Mann-Withney test. In case of multiple comparisons, False Discovery Rate (FDR) method has been used to correct p-values. Linear correlation was computed using Spearman's rho value. Significance level is set to 0.05.

5.3 Results

5.3.1 Differences between CIS/eRRMS and RRMS

The two clinical groups have show a few differences in Cortical Thickness: 5/33 left, 9/33 right cortical areas and 3/10 Lobes resulted significantly different; none of these differences survived FDR correction.
To the other side, aMRGlu differed in 13/33 L, 20/33 R areas and 11/14 lobes after correction. Lesion load was found significantly different in 4/33 L, 6/33 R and 6/14 Lobes for Lesion Number and 6/33 L, 4/33 R, 6/14 Lobes for Lesion Volume.

5.3.2 Grouping for lesion number

In order to better delineate differences, a second grouping criteria was added, selecting CIS/eRRMS with less than 70 WM+GM lesions and RRMS with more than 70 lesions. Resulting groups were made of 11 and 12 patient each.
Cortical thickness was found significantly different in 14(5 after correction)/33 Left VOIs, 15(5) Right and 5(1)/10 Lobes.
Absolute Glucose Rate differed in 21(10)/33 L, 28(12)/33 R and 13(8)/14 Lobes.

5.3.3 Correlations

Correlations were analyzed for Lobes, adding the Left and Right WM for noncortical measurements (all, excluded Cortical Thickness).
No significative correlation was found between Cth and aMRGlu in the cortical Lobes. To the other side, L WM aMRGlu. , inversely correlated with R and L Temporal and Insular Cth and R WM aMRGlu inversely correlated with the Cth of R Insular Lobe.

As concerns the relationship between Cth and Lesion Load, it was possible to find inverse correlations in L Frontal and Parietal Lobes and R Parietal and Temporal, both

considering lesion number and volume.
At last, inverse correlations were found between aMRGlu and lesion load in L/R Parietal, both considering volume and number of WM lesions.
In all the previous correlation, the Spearmann's rho value ranged in -0.3 and -0.5, which classifies them as mild correlations.

5.3.4 Voxelwise analysis

The mean aMRGlu of WM lesion was found as significantly lower ($p<0.01$) than the one of Normal Appearing WM (i.e. all WM excluding the Lesions VOI), while no significant difference was proven between GM lesions VOI and normal appearing GM ($p=0.18$). However, no precise pattern seems to arise from this images. As can be observed in Fig. 5.3Hisograms of the mean aMGLu values inside (green) and outside (blue) lesion masks in WM (left) and GM (right). This histograms is referred to the whole cohort of patients of this study.figure.caption.47, to a lesion VOI can correspond a lower (more frequently, especially in WM), normal or even higher aMRGlu value with respect to the surrounding normal appearing WM, see also Fig. 5.4An example of aMRGlu pixelwise map (right) and the corresponding T1 slice with WM (green) and GM (red) lesions in overlay (left). Note that a lesion can correspond to a lower (more frequently), a normal or even a higher aMRGlu value than the surrounding WM.figure.caption.48 and Fig. 5.5Another example of voxelwise aMRGlu map in a MS patient. A: T1-w axial slice of a patient; B: FLAIR; C: DIR; D: Voxel-wise map of MRGlu sampled at 2x2x2 mm resolution. All images were registered to D. Blue arrows: lesions with corresponding hypo-metabolism; red arrows: lesions with corresponding high MRglu values.figure.caption.49. This could be related to the presence or absence of an active inflammatory process in the area.

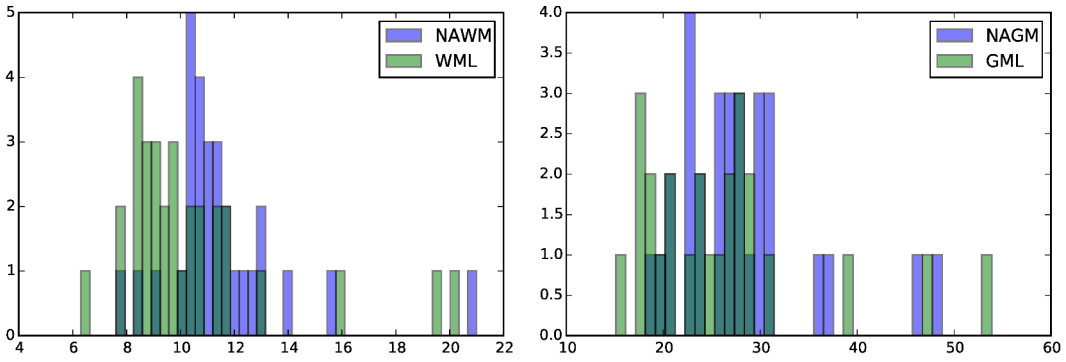

Figure 5.3: Hisograms of the mean aMGLu values inside (green) and outside (blue) lesion masks in WM (left) and GM (right). This histograms is referred to the whole cohort of patients of this study.

5.4 Discussion

The few significative differences between CIS/eRRMS and RRMS in CTh seems to be in countertrend with the findings of MS literature. However this result can be derived from our low sample number, which could not be sufficiently large to detect differences in CTh[10]. Some more significative differences have been found excluding some CIS/eRRMS with much lesions and some RRMS patients with lower lesion number.
From this cohort's results it is possible to hypothesize that aMRGlu may have an earlier change than atrophy (CTh) and focal lesion appearance, as aMRGlu differences between groups were significative in more areas. This result has to be checked with stronger data, as a longitudinal study.

The inverse correlations between aMRGlu and lesion load suggest that the metabolism of the brain is dependent to the inflammatory process, but differently from Cth. Indeed, the results given by voxelwise analysis, together with the absence of correlations between CTh and aMRglu, are suggestive of a non-linear relationship between metabolism, inflammation and neurodegeneration. The cortex of MS in early disease phases may go through different states of metabolic activity.
It is possible to formulate this hypothetical model, to be verified in further study:

1. In a first phase, pro-inflammatory cytokines released by activated microglia[6, 16, 17] lead to an increase of the synaptic metabolic rate.

2. In a second phase, the excitotoxic damage[3, 18, 19, 20] determines a progressive decrease in synaptic activity with a consequent decrease of metabolism, but still normal CTh.

3. Finally, in a third phase, the progressive loss of synapsis and the neuronal death determine the appearance of cortical atrophy.

It should be pointed out that all these conditions may take place in different areas at the same time. Hence only an accurate voxel-wise analysis can validate or reject such model.

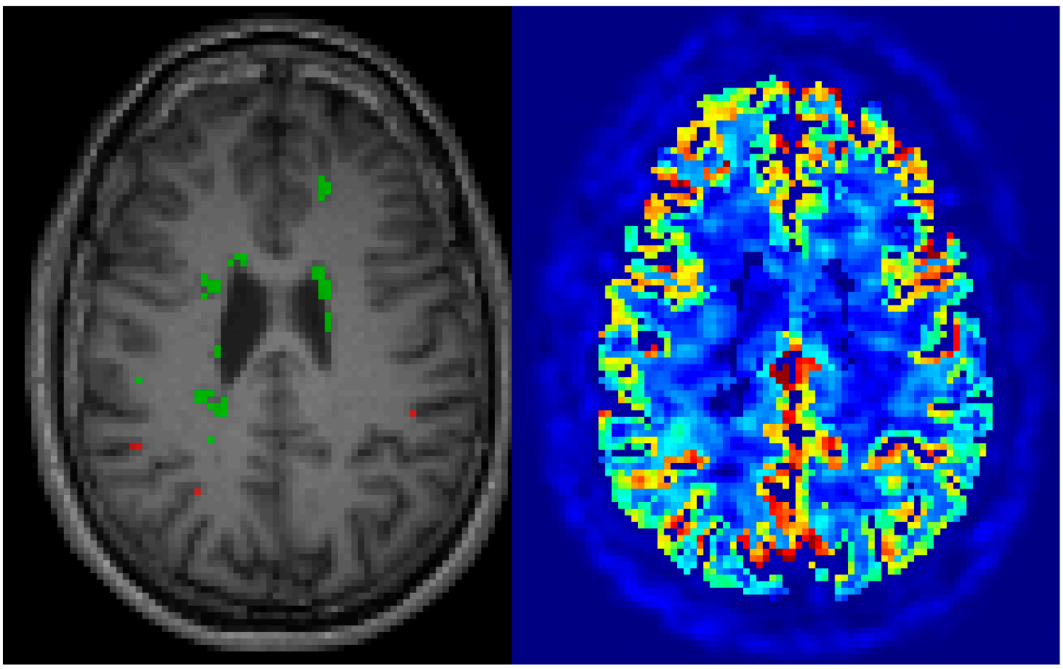

Figure 5.4: An example of aMRGlu pixelwise map (right) and the corresponding T1 slice with WM (green) and GM (red) lesions in overlay (left). Note that a lesion can correspond to a lower (more frequently), a normal or even a higher aMRGlu value than the surrounding WM.

5.5 Conclusions and Future Work

Various patterns of association between aMRglu and WM and GM pathology were observed in CIS/eRRMS and RRMS patients. The findings of this work indicate that cortical metabolism is a dynamic parameter especially in the early disease phases, probably linked to variable state of activation of both neurons and glial cells.

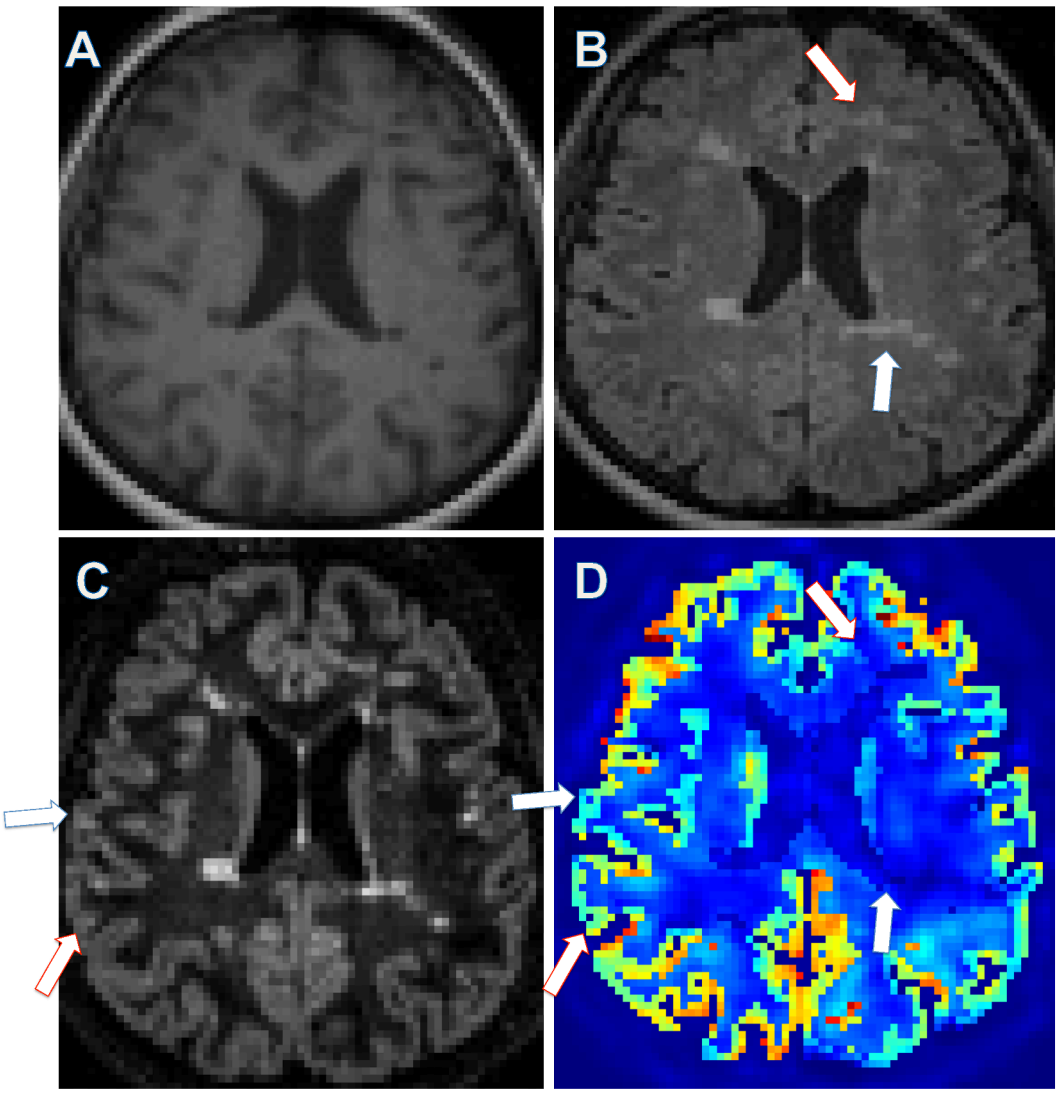

Figure 5.5: Another example of voxelwise aMRGlu map in a MS patient. A: T1-w axial slice of a patient; B: FLAIR; C: DIR; D: Voxel-wise map of MRGlu sampled at 2x2x2 mm resolution. All images were registered to D. Blue arrows: lesions with corresponding hypo-metabolism; red arrows: lesions with corresponding high MRglu values.

A follow-up for this study, currently in progress, will probably solve many of the questions posed by this work. Furthermore, adding a set of Healthy Control subjects would also help to define rigorously hyper- and hypo-metabolic areas, allowing to validate and refine our present findings.

Bibliography

[1] M Blinkenberg, CV Jensen, S Holm, OB Paulson, PS Sorensen, *A longitudinal study of cerebral glucose metabolism, MRI, and disability in patients with MS*, Neurology, 1999.

[2] M Blinkenberg, HK Mathiesen, T Tscherning, et al., *Cerebral metabolism, magnetic resonance spectroscopy and cognitive dysfunction in early multiple sclerosis: an exploratory study*, Neurol Res, 2012.

[3] J Gimeno-Bayon, A Lopez-Lopez, MJ Rodriguez, N Mahy, *Glucose pathways adaptation supports acquisition of activated microglia phenotype*, J Neurosci Res, 2014.

[4] DS Knopman, CR Jack, et al., *Selective worsening of brain injury biomarker abnormalities in cognitively normal elderly persons with β-amyloidosis*, JAMA Neurol, 2013.

[5] CR Jack, et al., *Amyloid-first and neurodegeneration-first profiles characterize incident amyloid PET positivity*, Neurology, 2013.

[6] J Jurcovicova, *Glucose transport in brain - effect of inflammation*, Endocr Regul, 2014.

[7] NW Lutz, A Viola, I Malikova, et al., *Inflammatory multiple-sclerosis plaques generate characteristic metabolic profiles in cerebrospinal fluid*, PLoS One, 2007.

[8] PJ Magistretti, *Neuron-glia metabolic coupling and plasticity*, J Exp Biol, 2006 Jun.

[9] F Nelson, S Datta, N Garcia, et al., *Intracortical lesions by 3T magnetic resonance imaging and correlation with cognitive impairment in multiple sclerosis*, Mult Scler, 2011.

[10] HR Pardoe, DF Abbot, et al, *Sample Size Estimates for Well-Powered Cross-Sectional Cortical Thickness Studies* Hum Brain Mapp, 2013.

[11] CH Polman, SC Reingold, B Banwell, et al., *Diagnostic criteria for multiple sclerosis: 2010 revisions to the McDonald criteria*, Ann Neurol, 2011 Feb.

[12] BF Popescu, RF Bunyan, JE Parisi, RM Ransohoff, CF Lucchinetti, *A case of multiple sclerosis presenting with inflammatory cortical demyelination*, Neurology, 2011 May 17.

[13] C Pozzilli, C Fieschi, D Perani, et al., *Relationship between corpus callosum atrophy and cerebral metabolic asymmetries in multiple sclerosis*, J Neurol Sci, 1992.

[14] U Roelcke, L Kappos, J Lechner-Scott, et al., *Reduced glucose metabolism in the frontal cortex and basal ganglia of multiple sclerosis patients with fatigue: a 18F-fluorodeoxyglucose positron emission tomography study*, Neurology, 1997.

[15] SD Roosendaal, K Bendfeldt, H Vrenken, et al., *Grey matter volume in a large cohort of MS patients: relation to MRI parameters and disability*, Mult Scler, 2011.

[16] S Rossi, R Furlan, Chiara De, et al., *Interleukin-1beta causes synaptic hyperexcitability in multiple sclerosis*, Ann Neurol, 2012 Jan.

[17] S Rossi, C Motta, V Studer, et al., *Interleukin-1β causes excitotoxic neurodegeneration and multiple sclerosis disease progression by activating the apoptotic protein p53*, Mol Neurodegener, 2014 Dec 12.

[18] IL Simone, F Federico, M Trojano, et al., *High resolution proton MR spectroscopy of cerebrospinal fluid in MS patients*, Comparison with biochemical changes in demyelinating plaques, J Neurol Sci 1996.

[19] C Stadelmann, *Multiple sclerosis as a neurodegenerative disease: pathology, mechanisms and therapeutic implications*, Curr Opin Neurol, 2011.

[20] BD Trapp, PK Stys, *Virtual hypoxia and chronic necrosis of demyelinated axons in multiple scle rosis*, Lancet Neurol, 2009.

[21] C Wegner, MM Esiri, SA Chance, J Palace, PM Matthews, *Neocortical neuronal, synaptic, and glial loss in multiple sclerosis*, Neurology, 2006.

Chapter 6

Amyloid PET/MRI analysis for AD

> One tended to speak of him, instinctively, as a spiritual casualty, a *lost soul*: was it possible that he had really been *desouled* by a disease?
> "Do you think he has a soul?" I once asked the Sisters. They were outraged by my question, but could see why I asked it. "Watch Jimmie in chapel", they said, "and judge for yourself."
>
> Oliver Sacks, *The Man Who Mistook His Wife For A Hat*

Alzheimer's Disease (AD), introduced in the first Chapter, is characterized by the excessive accumulation in the brain of beta-amyloid. Modern PET tracers are able to detect, quantify and localize this phenomenon with greater precision with respect to the analysis of Cerebrospinal Fluid CSF, extracted with a Lumbar Puncture (LP).
In this chapter a new study for PET quantification will be presented. The contents above are obtained with the collaboration of Department of Nuclear Medicine, Leipzig University DE, and the relative paper is currently in submission for publication.

6.1 Introduction

Amyloid accumulation is common in normal aging brain, but reaches abnormal levels in younger AD (between 60 and 70 years old). Amyloid level is not the only biomarker to consider for a precise diagnosis, but it is the earliest one that has been found. PET tracers as ^{18}F-Flutemetamol, ^{18}F-Fluorbetaben and ^{18}F-Fluorbetapir allow to detect the brain zones of amyloid accumulation, but also to quantify such phenomenon.
At present day clinical practice include PET imaging with one of the above tracer, which

is visually and qualitatively inspected by trained experts. The aim of the inspection is to exclude AD, otherwise the patient has to undergo other exams. Several semi-quantitative [3, 5, 6], quantitative [1, 8] or kinetics[2] methods have been proposed in the past.
In this work a quantitative method is proposed and compared with qualitative results. This method uses both early and late acquisitions in order to take kinetics into account. It has been applied to a particular tracer, but it can be applied to different amyloid tracers and can be helpful for qualitative assessments too.

6.2 Materials and Methods

6.2.1 Patients

A total number of 86 subjects was enrolled in the study, 53 negatives and 33 positives according to the qualitative analysis made by two independent experts. Conflicting cases were solved by a third independent expert. All patients gave written informed consent.

6.2.2 PET/MRI

PET static images were taken in two phases: an early phase PET1 and a later-acquired PET2. Only a T1-weighted MPRAGE MRI (MRI2) sequence was acquired concurrently to the latter PET. The motivation of this choice is to normalize for the uptake early phase of the tracer kinetics.

6.2.3 Pipeline

Since PET images available are static, the pipeline applied in this study is simpler to the one used in the previous Chapter, see Fig. 6.1Flowchart for the pipeline followed in this study. Edema segmentation was not included, as it only affects the decision about keeping or not the final aMRGlu value. For shake of simplicity also the registration of freesurfer-obtained atlas to BIC space is omitted.figure.caption.51. Instead of using a thoracic PET/MRI for computing the plasma glucose, now the average PET value per VOI is computed with SUVR using the cerebellar cortex as reference tissue.

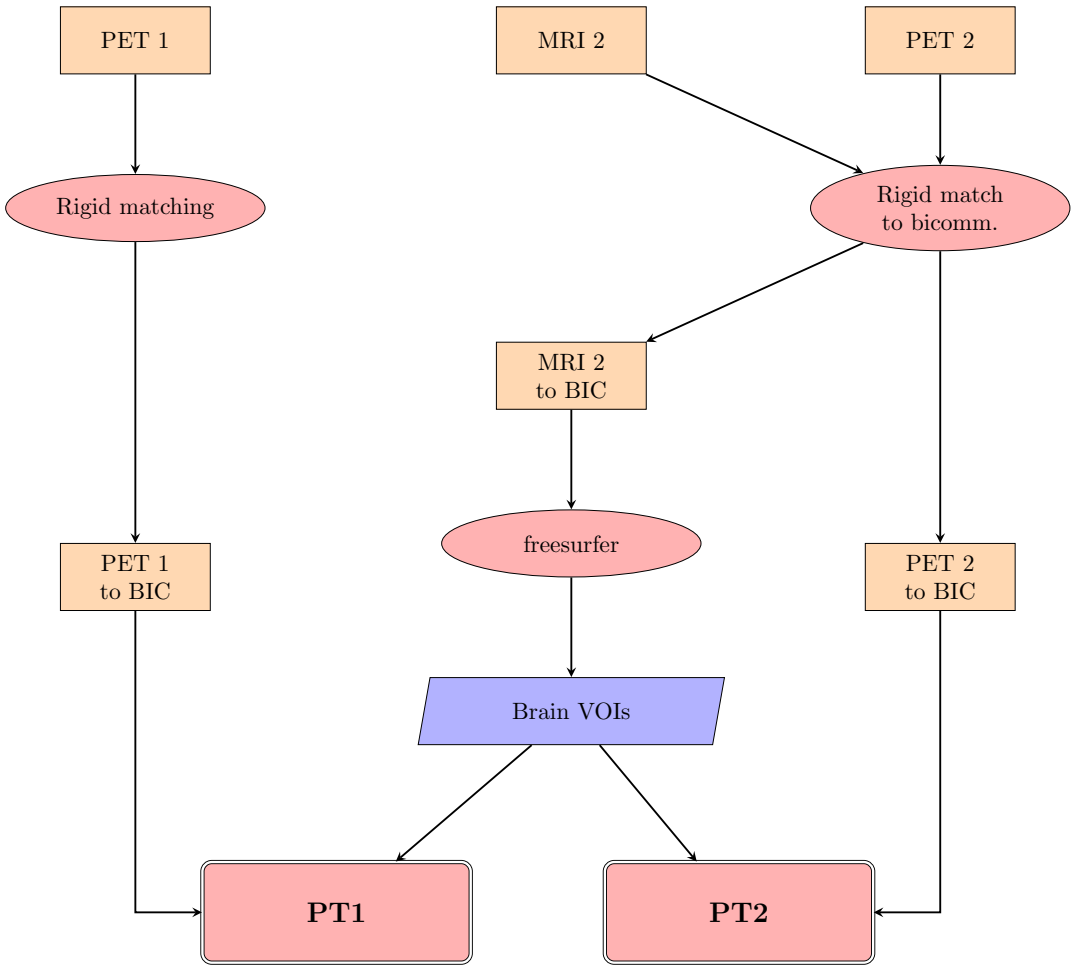

Figure 6.1: Flowchart for the pipeline followed in this study. Edema segmentation was not included, as it only affects the decision about keeping or not the final aMRGlu value. For shake of simplicity also the registration of freesurfer-obtained atlas to BIC space is omitted.

The resulting numerical value will be called

$$R_1 = \frac{PT1}{PT1(cerebellum\,ctx)}$$

for the early SUVR and

$$R_2 = \frac{PT2}{PT2(cerebellum\,ctx)}$$

for the later one.
Other biomarkers have been computed as the slope

$$R_{slope} = \frac{R_2 - R_1}{\Delta t}$$

where Δt is the difference in minutes between the early and the later acquisition, and the Relative WM Index (RWMI)

$$RWMI = 100\frac{PET2 - PET2(WM)}{PET1 - PET1(WM)}.$$

The idea between these last two indexes is to normalize the later PET values with respect to the uptake phase. The WM is taken as reference in RWMI because a recent publication[4] suggested that amyloid PET uptake in the cortex would greater than than WM uptake (so the denominator is likely to be positive), but later the PET in cortical areas would take values smaller than WM values in amyloid-negative subjects, differently from amyloid-positives. In a perfect-world enviromnent RWMI will plausibly be less than zero for negatives and greater than zero for positives. This does not always happen in practice. Nevertheless RWMI will be proven as a predictive biomarker in discern amyloid-positive and negative.
Other biomarkers as the Cortical Thickness for cortical VOIs and Volume in mm^3 come *for free* with using `recon-all` script from Freesurfer.

6.2.4 Statistics

When comparing two groups, their normality was checked using Shapiro-Wilk test. Then, the two groups were compared using unpaired t-test and Mann-Withney test. Linear correlation was computed using Spearman's rho value. Significance level was set to 0.01.

When testing a biomarker predictivity, K-means clustering was performed in scikit-learn0.16.
From the resulted predicted values of positivity (0 for negatively-predicted subjects, 1 for positive) True/False positive rates (tpr, fpr) were computed taking the expert's rate as reference. The relative Receiver Operator Curve (ROC) and its Area Under the Curve (AUC) was computed for Lobes. AUC is equal to 1 for the perfect predictor, 0.5 for the random guesser and 0 for the perfect liar.

Another method has been tried to guess positivity from biomarkers, Fig. 6.2Scheme for age-independent z-score.figure.caption.52. A biomarker y for a negative subject has been fitted with the subject's age x as $y = mx + q$ and the biomarker has been corrected for age, $y' = y - mx$. Mean and standard deviation μ, σ have been calculated for y'. A new subject's biomarker with value $\bar{y}$ and age $\bar{x}$ was then age-corrected $\bar{y}' = \bar{y} - m\bar{x}$ and its z-score was calculated as

$$z = \frac{\bar{y}' - \mu}{\sigma}.$$

If the z-score is high, say $z > 2$, the probability for this subject to be negative is neglectable and the subject can be rated as amyloid-positive.
This method has been tested on positive subjects's whole brain biomarkers to check how much of them would be rated as such.

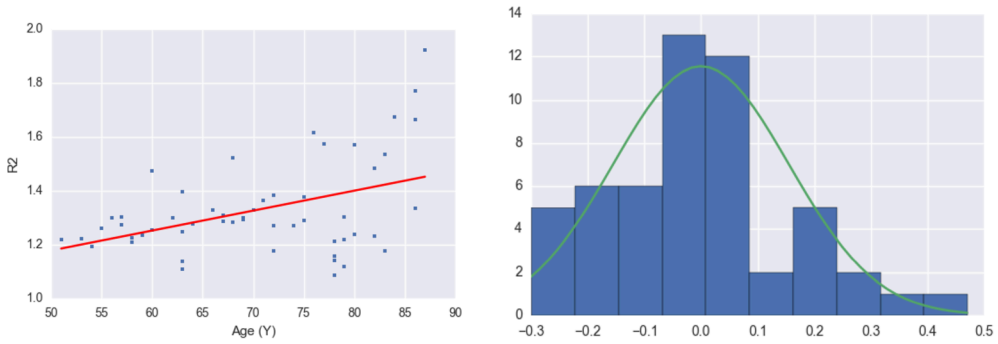

Figure 6.2: Scheme for age-independent z-score.

6.3 Results

No significative age difference was found between positive and negative groups. Significative differences between positive and negative groups were found in 1/68 areas (namely the left pars orbitalis) and 0/10 cortical lobes for CTh, 14/92 areas and 2/14 lobes for Volume. R_1 differed in few areas 7/92, and 1/14 lobes, while R_2 differed in 84/90 areas and 14/14 Lobes, R_{slope} in 81/90 areas and 14/14 Lobes $RWMI$ in 82/90 and 14/14 Lobes.
Predictivity analysis shown in Table 6.1Area Under the Curve (AUC) for the ROC of 6 Lobes and the TOTAL whole brain. Bigger values in red.table.caption.53 indicates in most of the cases R_2 as the most predictive biomarker. Only in one case $Rslope$ resulted better, and in three cases the two biomarkers predictivity resulted equivalent.

Correlation analysis showed that in negative subjects R_2, R_{slope} and $RWMI$ of the whole brain (p=.02 r=.31 for R_2, p=.002 r=.42 for R_{slope} and p=.0005 r=.46 for $RWMI$) and of the Lobes correlated with the age of the subjects, while this correlation has not been found in amyloid-positive group (p ~.5 and r~-.1 in whole brain).

Age-independent analysis has rated as positive 31/33 (94%) subjects for R_2 and R_{slope}, 25/33 (76%) of the subjects for $RWMI$.

Area	R_1 AUC	R_2 AUC	R_{slope} AUC	RWMI AUC
L FRONTAL	0.622	0.970	0.970	0.945
L INSULAR	0.605	0.960	0.951	0.941
L OCCIPITAL	0.522	0.835	0.790	0.780
L PARIETAL	0.539	0.951	0.945	0.890
L TEMPORAL	0.508	0.960	0.945	0.896
L CENTRAL	0.561	0.905	0.896	0.820
R FRONTAL	0.660	0.945	0.945	0.939
R INSULAR	0.618	0.945	0.923	0.936
R OCCIPITAL	0.563	0.854	0.854	0.845
R PARIETAL	0.543	0.934	0.915	0.915
R TEMPORAL	0.563	0.921	0.921	0.854
R CENTRAL	0.599	0.854	0.869	0.868
TOTAL	0.609	0.960	0.945	0.881

Table 6.1: Area Under the Curve (AUC) for the ROC of 6 Lobes and the TOTAL whole brain. Bigger values in red.

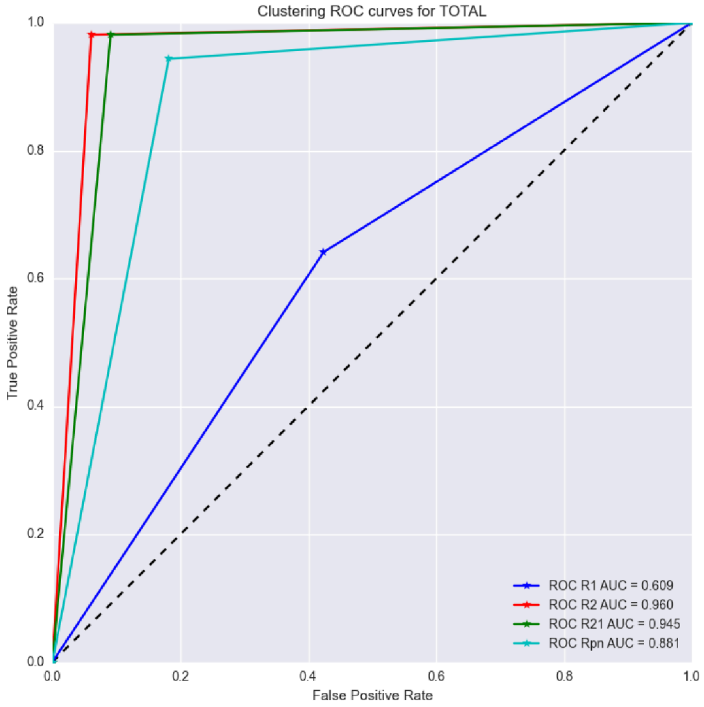

Figure 6.3: Receiver Operator Characteristic curves for the whole brain. Curves are shown for R_1 (blue), R_2 (red), R_{slope} (green), $RWMI$ (light blue).

6.4 Discussion

It is not strange that the differences in Cth (wich measures neurodegeneration) and R_1 (uptake) are not significative, as the age of the two groups is undistinguishable. The correlation of negative subjects' biomarkers with age proves that age-independent analysis, as in our description, is a reasonable choice. The R_2 biomarkers is in practice very similar to the criterium used by experts for rating PET images, and in fact it shows a better coherence with the assessment given. This does not necessarily mean that R_{slope} and $RWMI$ are actually less reliable in classifying between positive and negatives. It is interesting to observe for instance that R_{slope} shows in some negative subject higher value in areas that are histologically known to be early affected by abnormal amyloid accumulation as mesiotemporal, hippocampal and enthorinal cortex. In order to confirm such intuition however, a further study is needed.

6.5 Conclusions and Future Work

Cerebellar GM SUVR, or R_2 seems to delineate and predict amyloid positive vs negative group better than other biomarkers proposed in this work. However other biomarkers, obtained considering also the uptake phase, as R_{slope} or $RWMI$, have shown (especially the first one) a good predictivity and worths a further study in the future.

This work could benefit from longitudinal follow-up, in order to better delineate the ongoing biomarkers in normal aging as in AD patients. Another option in discussion is to extend such approach to PET/CT images, easier to find as the machine is more diffused in Italian Hospitals, with the drawback that in brain images CT are harder to segment in a reliable way than MRI.

Bibliography

[1] H Barthel, J Luthardt, et al., *Individualized quantification of brain β-amyloid burden: results of a proof of mechanism phase 0 florbetaben PET trial in patients with Alzheimer's disease and healthy controls*, Eur J Nucl Med Mol Imaging, 2011.

[2] GA Becker, M Ichise, H Barthel, et al. *PET quantification of 18F-florbetaben binding to β-amyloid deposits in human brains*, J Nucl Med, 2013.

[3] P Bourgeat, VL Villemagne, et al,, *Comparison of MR-less PiB SUVR quantification methods*, Neurobiol Aging, 2015.

[4] M Brendel, M HÃ¶genauer M, et al., *Improved longitudinal [(18)F]-AV45 amyloid PET by white matter reference and VOI-based partial volume effect correction*, Neuroimage, 2015.

[5] V Camus, P Payoux, et al., *Using PET with 18F-AV-45 (florbetapir) to quantify brain amyloid load in a clinical environment*, Eur J Nucl Med Mol Imaging. 2012.

[6] C Hutton, J Declerck, et al., *Quantification of 18F-florbetapir PET: comparison of two analysis methods*, Eur J Nucl Med Mol Imaging, 2015.

[7] N Nelissen, K Van Laere, et al., *Phase 1 study of the Pittsburgh compound B derivative 18F-flutemetamol in healthy volunteers and patients with probable Alzheimer disease*, J Nucl Med. 2009.

[8] L Saint-Aubert, F Nemmi, , et al., *Comparison between PET template-based method and MRI-based method for cortical quantification of florbetapir (AV-45) uptake in vivo*, Eur J Nucl Med Mol Imaging, 2014.

Chapter 7

High and Low Grade Brain Tumors in PET/MRI

> Not long after my grandmother died, my computer crashed and I lost the journal I had kept of her [...].
> I was ashamed of my need to translate into words the physical intimacy of her death, so while I was writing it, I took comfort in the fact that my journal did and did not exist. It lived in limbo, much as my grandmother had as she lay unconscious.
> But then my computer crashed and I wanted my words back. I mourned my journal alongside my grandmother. That secondary cyber loss brought back the first bodily loss and made it final. The details of her dying no longer lived in a safe interim computer sleep. My words were gone. Or were they? Friends who knew about such things assured me that in the world of computers, nothing is ever really gone.
>
> Jonathan Rosen, *The Talmud and the Internet*

High grade Brain Tumors can lead to patient passing out in a relatively short time[4, 3]. The treatment, consisting in neurosurgery, radiotherapy and chemotherapy can extend the survival time by some months. All the steps of the treatment rely on Imaging for detecting the tumor, studying a strategy for surgery and detecting post-surgery tumor relapses[2, 7, 6, 5]. This chapter contains a longitudinal study involving 12 patient, with pre- and post-surgery PET/RM images.

7.1 Introduction

After neurosurgery, the patient affected by brain tumor recovers cognitively and clinically. The aim of this study is to examine pre- and post-surgery PET/MRI with ^{18}Fdg tracer in order to observe the areas in with aMRGlu increases after the surgical intervention.

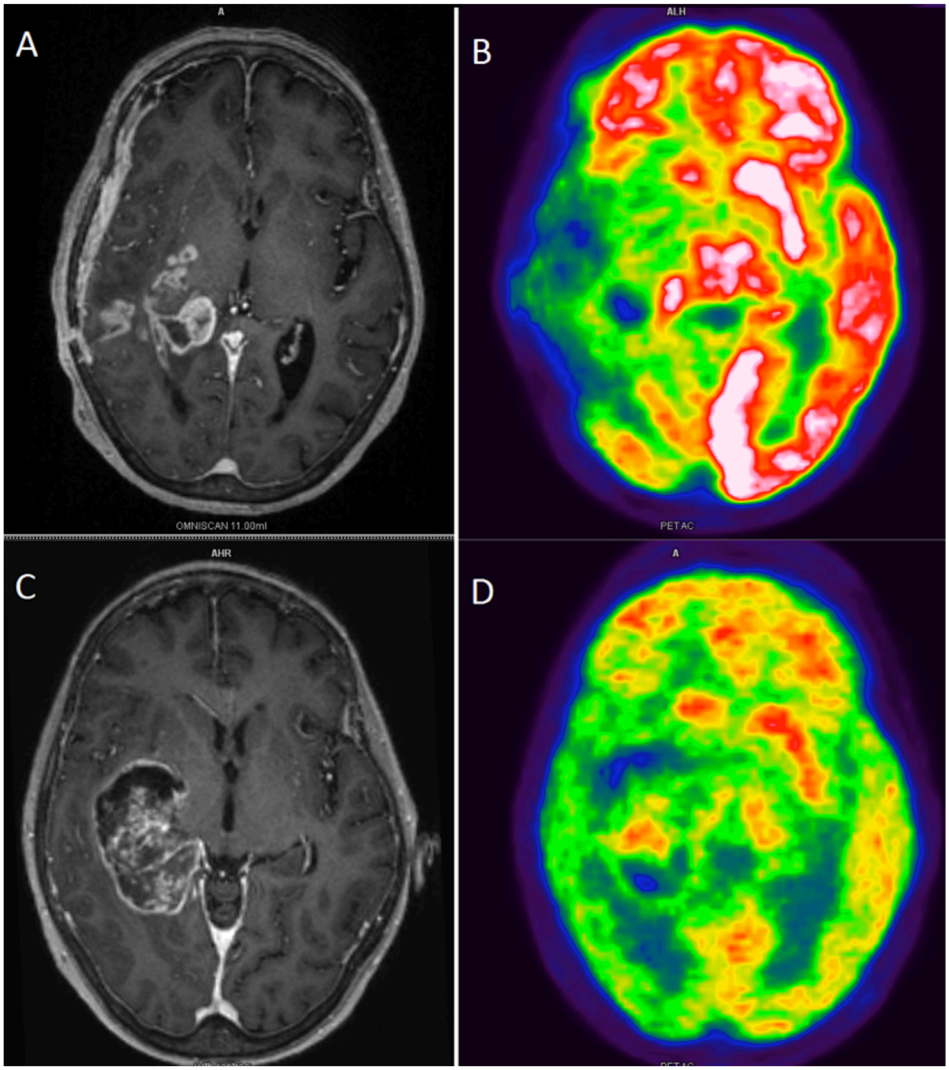

Figure 7.1: An example of PET/MRI before (C and D) and after (A and B) surgical intervention. It is possible to appreciate the growth in aMRGlu, expecially in the contralateral hemisphere.

7.2 Materials and Methods

7.2.1 Patients

Twelve patients were enrolled in the study, 8 with high-grade brain tumor, 4 with low grade. All patients gave written informed consent. Baseline was a week before intervention, and follow-up scan a month after surgery.

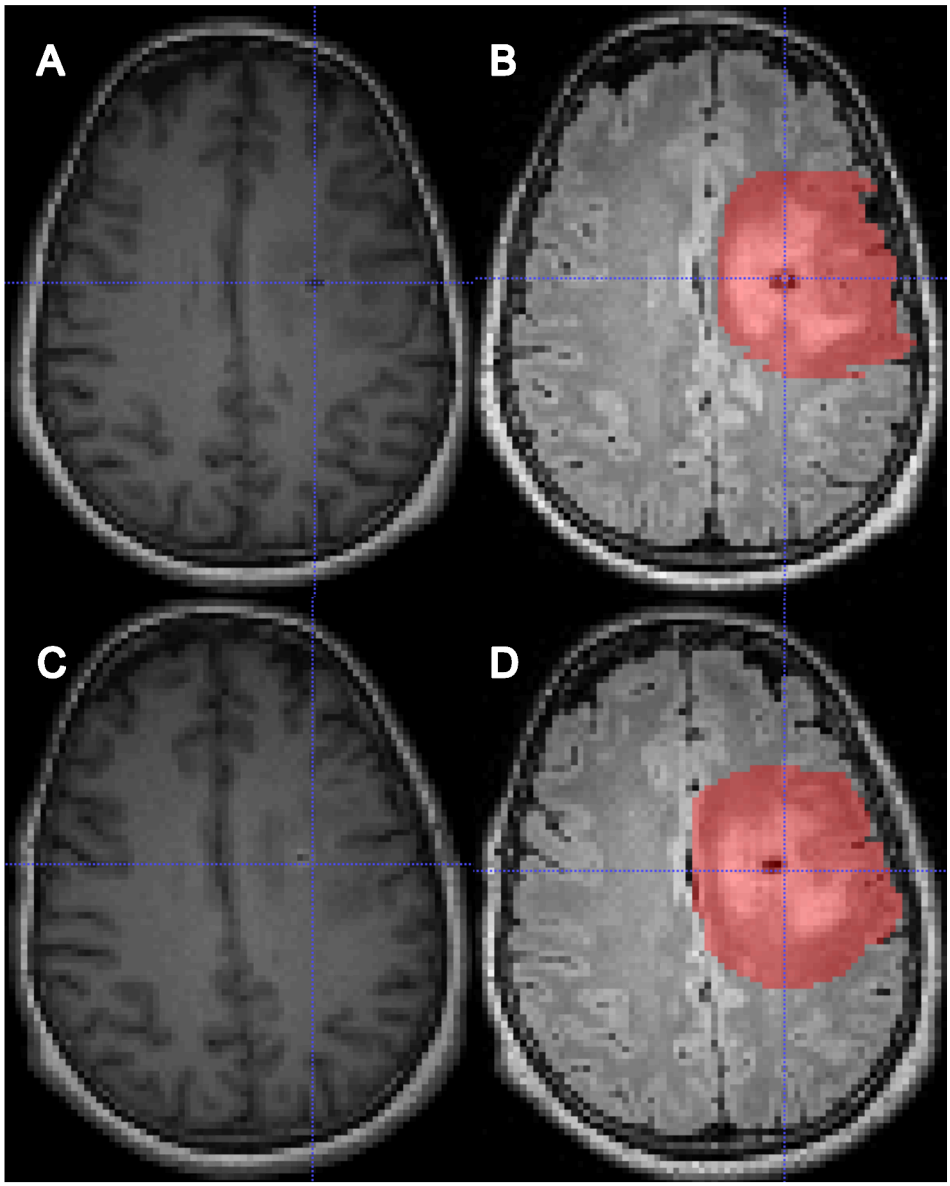

Figure 7.2: A MRI T1 (left) and aligned FLAIR (right) with edema VOI (in red overlay), before (A,B) and after (C,D) surgical intervention.

7.2.2 PET/MRI

Similarly to SM study, T1 and FLAIR sequences of the brain and STIR of the thorax were acquired for each patient at each session. Two PET scans in thorax and brain were acquired to compute plasma glucose with good precision. The scanning protocol was identical to the one explained in SM study, except that DIR sequence was not preformed.

7.2.3 Pipeline

Also the pipeline, Fig. 7.3Flowchart for the pipeline followed in this study. Edema segmentation was not included, as it only affects the decision about keeping or not the final aMRGlu value.figure.caption.58 was similar to the one used in MS study, with three main differences:

1. Instead of lesion segmentation, edema and tumor lesion area was manually segmented from FLAIR sequence. This mask was used to exclude areas with a percentage of edema greater then 5% and to automatically detect homo-lateral and contra-lateral hemispheres of the brain[1]. The surrounding area was included in the VOI to avoid mistaking tumor uptake for normal brain activity, see fig. 7.2A MRI T1 (left) and aligned FLAIR (right) with edema VOI (in red overlay), before (A,B) and after (C,D) surgical intervention.figure.caption.57.

2. Due to the presence of the tumor, automated softwares for brain segmentation would likely fail. It was chosen instead to use a probabilistic atlas defined in MNI152 space, over 37 healthy subjects. The chosen atlas was Fsl Harvard Oxford Lateralized Cortical (HOLC) Atlas[1], consisting in 48 left/48 right cortical labels and 20 left/20 right subcortical labels. The T1 MRI image was registered to the template MNI152, and the inverse registration was applied to HOLC Atlas. The resulting Atlas was used for PVC of the aligned PET image.

3. The probabilistic HOLC Atlas was converted to a simple, deterministic atlas, using the maximum probability criterium, explained in Eq. 4.1A formal introductionequation.4.1.1 with threshold equal to 0.1; the resulting VOIs were used to measure PET signal and the Patlak method was used to obtain aMRGlu for each VOI of the Atlas.

[1] for instance, if the edema area was in the left part of the brain, left hemisphere of the brain was the homo- and right hemisphere the contra-lateral.

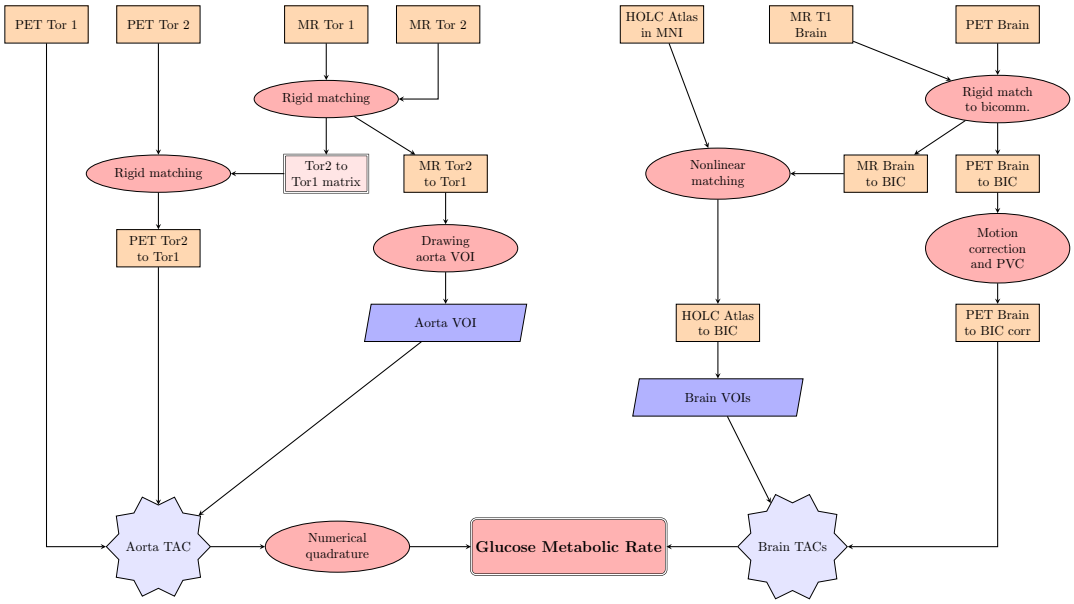

Figure 7.3: Flowchart for the pipeline followed in this study. Edema segmentation was not included, as it only affects the decision about keeping or not the final aMRGlu value.

7.2.4 Statistical Analysis

When comparing two groups, their normality was checked using Shapiro-Wilk test. Then, the two groups were compared using unpaired t-test and Mann-Withney test.

7.3 Results

Contralateral hemisphere has resulted to benefit from the intervention more than homolateral: as can be observerd in Table 7.1Mean values and p-values before-after neurosurgery in contralateral (left) and homolateral hemispheres. In red, the significative p-values, less than 0.05.table.caption.59, 13/48 cortical areas have significantly increased aMRGlu values. No significant increase has been found in homolateral hemisphere, except for Cuneal Cortex. Considering the different tumor grading, in 5/8 high grades and 3/4 it is possible to observe a increase of aMRGlu in all 48/48 cortical areas.

7.4 Discussion

This study confirms, in the limits of the low statistical sample size, the positive effects of surgical intervention in brain tumors. Surprisingly, contralateral hemisphere seem

Cortical Brain Region	Contr. Pre	Contr. post	p-val	Homol. pre	Homol. post	p-val
Frontal pole.	11.206	14.260	0.124	12.317	12.798	0.791
Insular Cortex	17.174	20.438	0.136	18.184	17.993	0.975
Superior Frontal Gyrus	15.142	18.237	0.149	14.993	17.827	0.295
Middle Frontal Gyrus	14.538	17.813	0.150	14.402	17.658	0.239
Inferior Frontal Gyrus, pars triang.	12.541	16.306	0.091	12.738	13.566	0.684
Inferior Frontal Gyrus, pars operc.	12.999	17.892	0.037	13.964	15.625	0.590
Precentral Gyrus	13.679	17.219	0.066	15.510	17.989	0.387
Temporal Pole	9.890	12.129	0.130	9.243	10.901	0.297
Superior Temporal Gyrus, anterior division	12.594	15.149	0.228	11.968	13.110	0.605
Superior Temporal Gyrus, posterior division	13.296	16.712	0.05	12.872	14.639	0.598
Middle Temporal Gyrus, anterior division	11.389	14.593	0.07	11.926	13.369	0.559
Middle Temporal Gyrus, posterior division	12.073	15.425	0.084	11.711	13.173	0.393
Middle Temporal Gyrus, temporooccipital part	12.563	16.451	0.044	11.950	14.814	0.278
Inferior Temporal Gyrus, anterior division	10.717	15.149	0.07	9.663	12.632	0.119
Inferior Temporal Gyrus, posterior division	10.393	14.652	0.04	10.335	12.171	0.310
Inferior Temporal Gyrus, temporooccipital part	12.294	15.806	0.094	11.971	14.304	0.341
Postcentral Gyrus	13.739	17.581	0.068	13.819	17.165	0.298
Superior Parietal Lobule	14.075	18.100	0.063	14.820	17.819	0.224
Supramarginal Gyrus, anterior division	11.877	14.714	0.114	10.626	12.514	0.507
Supramarginal Gyrus, posterior division	12.795	15.764	0.096	11.761	15.873	0.208
Angular Gyrus	13.733	17.461	0.067	13.508	15.840	0.429
Lateral Occipital Cortex, superior division	13.317	16.344	0.112	12.048	13.645	0.461
Lateral Occipital Cortex, inferior division	12.357	15.047	0.152	10.835	14.488	0.173
Intracalcarine Cortex	15.680	19.470	0.143	18.823	18.017	0.522
Frontal Medial Cortex	14.625	20.398	0.050	15.184	17.259	0.380
Juxtapositional Lobule Cortex	16.070	21.260	0.062	15.602	18.967	0.216
Subcallosal Cortex	14.666	17.416	0.172	13.928	16.701	0.156
Paracingulate Gyrus	17.134	20.458	0.204	18.245	17.520	0.801
Cingulate Gyrus, anterior division	11.732	16.418	0.023	14.015	15.759	0.404
Cingulate Gyrus, posterior division	14.593	19.542	0.048	15.223	17.714	0.487
Precuneous Cortex	16.373	20.476	0.086	13.385	18.549	0.139
Cuneal Cortex	16.923	22.428	0.066	14.111	20.973	0.014
Frontal Orbital Cortex	13.184	18.354	0.025	13.617	16.062	0.281
Parahippocampal Gyrus, anterior division	11.665	14.791	0.07	11.129	13.183	0.286
Parahippocampal Gyrus, posterior division	14.314	17.365	0.069	13.526	15.917	0.446
Lingual Gyrus	14.607	19.149	0.05	13.668	17.262	0.318
Temporal Fusiform Cortex, anterior division	8.158	11.722	0.044	7.882	9.832	0.324
Temporal Fusiform Cortex, posterior division	10.442	14.442	0.033	10.729	13.060	0.340
Temporal Occipital Fusiform Cortex	16.041	20.085	0.046	15.750	18.780	0.438
Occipital Fusiform Gyrus	15.364	19.849	0.051	14.920	18.709	0.225
Frontal Operculum Cortex	15.970	19.363	0.09	15314	18.099	0.572
Central Opercular Cortex	14.760	17.398	0.132	12.976	16.629	0.500
Parietal Operculum Cortex	13.538	16.867	0.041	14.861	16.360	0.767
Planum Polare	11.542	17.091	0.007	11.722	14.934	0.316
Heschl's Gyrus (includes H1 and H2)	19.193	27.918	0.008	17.811	25.257	0.127
Planum Temporale	17.950	24.699	0.030	17.621	20.259	0.569
Supracalcarine Cortex	18.458	22.267	0.284	20.020	21.082	0.855
Occipital Pole	10.300	12.233	0.205	8.780	10.786	0.196

Table 7.1: Mean values and p-values before-after neurosurgery in contralateral (left) and homolateral hemispheres. In red, the significative p-values, less than 0.05.

to take advantage more than homolateral hemisphere of this effect. This can be interpreted as follows: the tumor mass requires much of the glucose and its pressure has effect in all the brain. After surgical intervention, the glucose of all the brain has a reprise, in particular the contralateral hemisphere; more than a local effect the reduction of pressure and of the edema has a global effect.

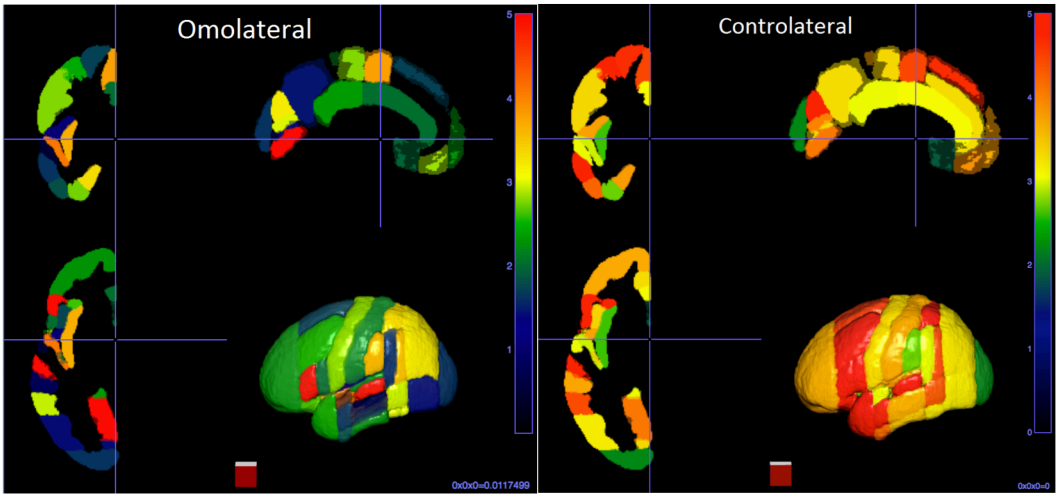

Figure 7.4: Mean values of difference beween post- and pre- intervention aMRGlu values in homo (left) and contra (right) lateral hemispheres. Notice that the difference is higher in contralateral.

7.5 Conclusions and Future Works

The acquisition or more subjects is currently in progress. Pre and post chemo and radiotherapy scans are also in progress in order to have a complete survey over treatment process.

Bibliography

[1] RS Desikan, F Sègonne, et. al, *An automated labeling system for subdividing the human cerebral cortex on MRI scans into gyral based regions of interest*, Neuroimage, 2006.

[2] L Douw, et al. *Cognitive and radiological effects of radiotherapy in patients with low-grade glioma: long-term follow-up*, Lancet Neurol. 2009.

[3] A Hutter, KE Schwetye, AJ Bierhals, RC McKinstry, *Brain neoplasms epidemiology, diagnosis, and prospects for cost-effective imaging*, Neuroimaging Clin N Am, 2003.

[4] Y Kienast, F Winkler, *Therapy and prophylaxis of brain metastases*, Expert Rev Anticancer Ther. 2010.

[5] YY Lee, P Van Tassel, *Intracranial oligodendrogliomas: imaging findings in 35 untreated cases*, AJR Am J Roentgenol. 1989.

[6] PE Ricci, *Imaging of adult brain tumors*, Neuroimaging Clin N Am, 1999.

[7] R Stupp , WP Mason, MJ van den Bent, et-al., *Radiotherapy plus concomitant and adjuvant temozolomide for glioblastoma*, N. Engl. J. Med, 2005.